Acta Materialia 276 (2024) 120106

Contents lists available at ScienceDirect

Acta Materialia

journal homepage: www.elsevier.com/locate/actamat

Full length article

Plastic deformation delocalization at cryogenic temperatures in a nickel-based superalloy

Dhruv Anjaria [a,*], Milan Heczko [b], Rephayah L. Black [a], Chris Bean [a], Mike A. Reynolds [c], Kun Zhang [c], Damien Texier [d], Valery Valle [e], Michael J. Mills [b], Darren C. Pagan [f], J.C. Stinville [a,*]

[a] *University of Illinois Urbana-Champaign, Urbana, IL, USA*
[b] *The Ohio State University, Columbus, OH, USA*
[c] *Shell Company, Houston, TX, USA*
[d] *Institut Clement Ader (ICA) - UMR CNRS 5312, Université de Toulouse, CNRS, INSA, UPS, Mines Albi, ISAE-SUPAERO, Albi, France*
[e] *Institut PPRIME, Université de Poitiers, CNRS, ENSMA, Chasseneuil, France*
[f] *The Pennsylvania State University, University Park, PA, USA*

ARTICLE INFO

Keywords:
Cryogenic temperatures
Plastic deformation delocalization
Nickel-based superalloy
High-resolution digital image correlation
Nanotwinning

ABSTRACT

A nickel-based superalloy is examined during monotonic deformation from ambient to cryogenic temperatures, reaching as low as liquid helium temperature. A detailed multimodal analysis of the microstructure and plasticity is conducted to discern changes in deformation mechanisms and plastic deformation localization under cryogenic conditions. This study employs high-resolution digital image correlation and transmission electron microscopy to identify the deformation mechanisms and understand their influence on plastic deformation localization as the temperature varies. At cryogenic temperatures, unusual plastic deformation localization processes are observed, attributed to the competing activation of a range of deformation processes. Furthermore, a mechanism of slip delocalization, i.e., local plastic deformation homogenization through closely spaced slip, is noted at these extreme temperatures. Ultimately, the impact of the microstructure is identified across the temperature range, from room to cryogenic temperatures.

A **colorblind-friendly version** (protanopia, deuteranopia, tritanopia) is provided in supplementary materials. Figures were remade using the ImageJ “Replace Red with Magenta” plug-in under the Image>Color menu, see Ref. [1]., the use of the Parrot LUT, see Ref. [2], and through custom edits.

1. Introduction

Structural metallic materials for cryogenic environments are emerging as key enablers and will be transformational for industries in energy, such as cryo-compressed storage for liquid hydrogen [3], and space exploration-focused applications [4,5]. Particularly, high-strength materials such as superalloys and titanium alloys, along with lightweight materials like aluminum and titanium alloys, are of renewed interest for cryogenic applications in the domains of space and energy storage and delivery, where conventional stainless steels are not suitable. These metallic materials often exhibit drastically different macroscopic mechanical properties at cryogenic temperatures compared to ambient or elevated temperatures [6–12], and the origins of these changes in behavior at the microstructure scale are broadly unknown.

Dislocation slip is typically the primary mechanism responsible for plastic deformation for face-centered cubic (FCC) materials under conventional conditions. However, when loading occurs in extreme conditions, such as at high strain rates, high deformation, or low temperatures, dislocation motion may become erratic, and deformation twinning may become the dominant mode of plasticity [13–16]. More importantly, often conditions exist where deformation twinning and dislocation slip coexist, inducing complex deformation mechanism interactions [17–19] giving rise to beneficial [11] or detrimental mechanical properties [18]. Challenges exist to predict how plasticity will be divided between the deformation twinning and dislocation slip mechanisms. For instance, in the context of twinning-induced plasticity (TWIP) steels, it is understood that the relative inputs of deformation twinning and dislocation slip change throughout the phases of work hardening, making prediction and characterization of deformation interaction complex [20,21]. Beyond this, there are further material systems, such as nanotwinned materials [22] and high entropy alloys (HEA) [23,24], where the progression of competition between

* Corresponding authors.
E-mail addresses: anjaria3@illinois.edu (D. Anjaria), jcstinv@illinois.edu (J.C. Stinville).

https://doi.org/10.1016/j.actamat.2024.120106
Received 20 March 2024; Received in revised form 11 June 2024; Accepted 11 June 2024
Available online 18 June 2024

these mechanisms is crucial to understand mechanical properties of these alloys. In parallel, when considering polycrystalline materials, the heterogeneities of the microstructure play an important role that further complexifies the understanding of these deformation mechanisms' interactions.

To fully comprehend the impact of microstructure heterogeneities on metallic materials and the interactions between deformation twinning and dislocation slip, it is essential to characterize these deformation events statistically and quantitatively. In recent decades, novel experimental tools have been developed to analyze dislocation slip in representative microstructure regions, providing new insights into the role of microstructure on the deformation and mechanical properties of metals [25–37]. For instance, high-resolution digital image correlation can rapidly identify slip events [38–40] or deformation twinning [41] at the nanometer scale in correlation with the grain structure of the material. Such statistical measurements have established important links between dislocation slip or deformation twinning, plastic deformation localization, and mechanical properties [41–48].

However, these tools are limited in identifying the competition between dislocation slip and deformation twinning. While slip involves sliding one plane of atoms over another, twinning produces a planar defect in the form of a twinned region that can span from a few atomic planes to significantly larger regions [49]. The twinned region in FCC materials can be considerably small [11,18], making it challenging to identify and differentiate from dislocation slip without advanced high-resolution electron microscopy techniques. Therefore, a statistical view of these different deformation events across representative microstructure regions is usually prevented.

The current work presents the implementation of high-resolution digital image correlation (HR-DIC) measurements to provide quantitative and statistical measurements of both dislocation slip and deformation twinning and identify competing deformation mechanisms. An advanced DIC method, Heaviside-DIC [38], developed initially to quantify dislocation slip, is implemented to quantify both deformation twinning and dislocation slip simultaneously. Complemented and supported by multi-scale electron microscopy based characterization down to atomic resolution, this novel method is utilized to identify the role of the microstructure and plastic deformation localization behavior at cryogenic temperatures of a nickel-based superalloy, Inconel 718, which has been considered for space applications along with handling and containment of high pressure cryogenic fluids owing to its high strength [50]. In addition, Inconel 718 is the most widely used superalloy [51], the material studied presently has been given a conventional heat treatment such that both γ' and γ" strengthening precipitates are present. Recent work on 718 [52] and Co-based γ'/γ" strengthened superalloy [53] after room temperature deformation indicates pronounced activity of stacking fault shearing and twinning/micro twinning at larger strains indicating complex interaction between slip and twinning. There is little understanding of the mechanical behavior and deformation modes of this precipitate-strengthened condition at cryogenic temperatures where this interaction can be more pronounced.

Mechanical stresses and thermal fluctuations control the activation of the deformation mechanisms and processes in a given material. The activation of these deformation processes depends on the applied stress as well as the available thermal energy. At cryogenic temperatures, the thermal component is reduced, due to which the applied stress has to be increased in order to lower the stress-dependent activation energy for different deformation mechanisms [17,54]. With increasing applied stress, the activation energy differences between deformation processes become much smaller. Consequently, unique and often competing deformation mechanisms are observed at cryogenic temperatures [17,55]. It follows that many stress-driven deformation mechanisms, such as dislocation slip, deformation twinning, cross-slip, and multiple-slip activation from grain boundaries, can collectively accommodate plastic deformation [17] and generate plastic deformation localization that is not observed during ambient temperature deformation. Another seldomly examined deformation process occurs at cryogenic temperatures when most FCC materials exhibit unique macroscopic properties as they near the temperature of absolute zero. A discontinuous plastic flow is observed, significantly altering the properties of the material, originating from a transition from screw to edge dislocation glide [56]. The impact of all of these processes on plastic deformation localization is presently identified in the investigated nickel-based superalloy. An unexpected phenomenon of slip delocalization at cryogenic temperatures is observed, which is related to the lower activation energy differences between deformation processes.

2. Experimental details

All collected electron microscopy images used for HR-DIC measurement and the associated mechanical behavior responses at different investigated temperatures for the investigated material are provided in the data repository Dryad [57].

2.1. Material

The present study investigated a nickel-based superalloy, Inconel 718. The Inconel 718 material had a nearly random texture and was subjected to an annealing treatment at 1050 °C for 30 min, followed by water quenching to produce a grain size distribution centered at 65 μm. The grain size analysis included annealing twins. The obtained grain structure is shown in Fig. 1(c) using an inverse pole figure map. The annealing treatment was conducted above the delta solvus. Subsequently, a two-step precipitation hardening treatment was performed by subjecting the material to 8 h at 720 °C, followed by 8 h at 620 °C. This treatment resulted in the formation of hardening γ' and γ" precipitates [58–60].

2.2. Mechanical testing

Flat dogbone-shaped specimens were prepared for testing with a gauge section measuring 1 × 3 mm^2 as shown in Fig. 1(a). The tensile specimens were cut by wire electrical discharge machining and mechanical mirror polishing using abrasive papers and diamond suspensions. Additionally, chemo-mechanical polishing was carried out using a suspension containing 0.05 μm colloidal silica particles.

A few specimens were then subjected to mechanical testing at room temperature using a NewTec Scientific™ MT1000 5000 Newton tensile stage. The other specimens were subjected to mechanical loading using an electromechanical 3R™ VHCF MEG20TT frame equipped with a custom setup for cryogenic testing. The cooling system consists of a vacuum double-walled chamber, multilayer insulation material, and helium/nitrogen liquid container. The system is designed as a closed-loop to recycle helium and is displayed in Fig. 1(b). The specimens are exposed to either liquid helium or nitrogen pushed from a dewar using helium or nitrogen gas, respectively. The temperature measurement was conducted using a silicon diode located near the specimen that displays an accuracy of less than 1 Kelvin within a range of 1.4 to 500 Kelvin. Temperature values of 77 K ± 2 K were obtained for tests labeled as liquid nitrogen temperature. Significant variability in temperature was observed for tests labeled liquid helium temperature. All temperatures were recorded significantly below 77 K, with observations reaching as low as 9 K ± 2 K.

The monotonic tensile tests were conducted at a quasi-static strain rate between 10^{-5} s^{-1} to 10^{-4} s^{-1}. The engineering stress–displacement curves obtained at the different temperatures are displayed in Fig. 1(d). As indicated by the inset in Fig. 1(d), significant stress drops are observed in the plastic regime for the test conducted at liquid helium temperature, also referred to as serrated yielding or low-temperature serrated deformation, which is mentioned for FCC materials close to absolute zero temperature [61–65]. It is also noted that this behavior

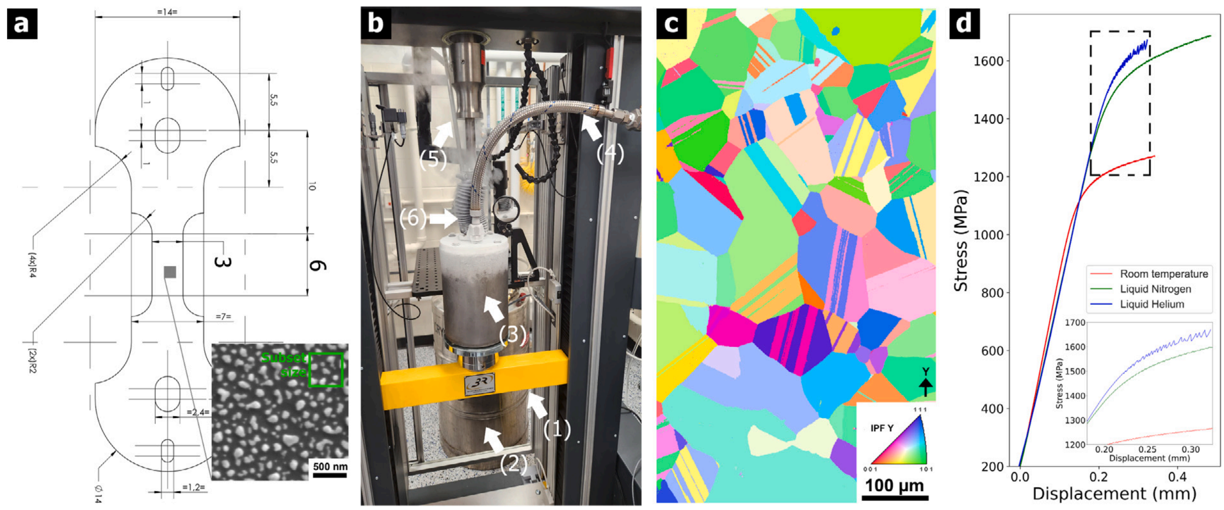

Fig. 1. Experimental setup for cryogenic temperature testing with ex-situ high-resolution digital image correlation measurement (a) Sample geometry used for mechanical testing. Dimension provided in millimeters. The thickness of the specimens was 1 mm. A scanning electron image of the speckle pattern used for HR-DIC is provided in the inset. **(b)** Experimental setup for mechanical loading at liquid helium temperature. (1) Moving traverse for mechanical loading equipped with a 20kN cell force; (2) liquid helium dewar; (3) vacuum double-walled chamber with thermal isolation; (4) recycling line for helium gas; (5) liquid helium transfer line; (6) impervious flexible to seal chamber. **(c)** Inverse pole figure along the vertical direction, obtained by electron backscatter measurements, showing the grain structure of the investigated material. **(d)** Engineering stress–displacement curves at liquid helium (LHe), liquid nitrogen (LN_2), and room temperature for the investigated material.

is not observed for the test conducted at liquid nitrogen temperature, thereby highlighting the difference in macroscopic tensile behavior as the temperature is lowered significantly. Several specimens were used for high-resolution electron microscopy based characterization and measurements and deformed at room temperature to 0.61% and 1.22% of plastic deformation, at liquid nitrogen temperature to 0.65%, 0.83%, 1.53% and 3.86% and at liquid helium temperature to 0.88%, 0.99% and 1.86% of plastic deformation. The applied plastic strains were obtained by averaging the ϵ_{xx} strain along the loading direction measured from HR-DIC. 0.2% offset yield strengths of 1071 MPa, 1362 MPa, and 1470 MPa are obtained at room, liquid nitrogen, and liquid helium temperatures, respectively.

2.3. Electron microscopy

Scanning electron microscopy (SEM) characterization was performed using a Thermo Fisher Scientific™(TFS) Scios Dual Beam SEM with a field emission gun (FEG). The imaging was conducted over areas with dimensions of 1076x1030 µm^2, using a 9 × 13 grid pattern with 15 % overlap between neighboring images. The imaging was performed at an accelerating voltage of 10 kV and a current of 0.80 nA. The images were acquired with a dwell time of 10 µs, with a horizontal field width of approximately 138 µm, at a working distance of 5 mm. The resulting images had a pixel resolution of 6144 px × 4096 px. Automated imaging was performed using the AutoScript software from ThermoFisher™and a custom Python routine for automated focus/astigmatism and grid imaging before and after deformation. The Python routine has been made available on GitHub (https://github.com/cmbean2/Automated-SEM-Procedure).

Electron backscatter diffraction (EBSD) analyses were performed at a 70° tilt using a step size of 1 µm, square grid collection, 200 frames per second acquisition, an accelerating voltage of 30 kV and a current of 6.4 nA before deformation on the region investigated by HR-DIC. EBSD was performed on a TFS Scios2 Dual-Beam using a Hikari Super EBSD detector. EBSD maps were adjusted by distortion to match HR-DIC with pixel resolution using the method described in Ref. [66].

The deformation processes and the profiles of slip step that develop during deformation on the surface were observed and documented with the underlying microstructure using site- and orientation-specific TEM surface lamella preparation by focused ion beam (FIB). A TFS Helios SEM-FIB Dual-Beam system was used to extract the thin foils with a final cleaning at 5 kV and a current of 16 pA. A JEOL 2010 LaB6 transmission electron microscope (TEM) was used to capture conventional TEM images for surface extrusion analysis of these foils. Microstructure and defect analysis from these foils were performed using S-CORR probe aberration-corrected and monochromated TFS Themis-Z scanning electron microscope (STEM) at an acceleration voltage of 300 kV. STEM diffraction contrast imaging (DCI) was performed with bright-field (BF) and high-angle annular dark-field (HAADF) detectors by selection of the appropriate camera length [67]. Atomic resolution of the microstructure was performed by tilting the thin foils into specific low-index crystallographic zones. Data was collected and processed using TFS Velox software. STEM micrographs were corrected for potential sample drift and scanning beam distortions using the drift-corrected frame integration function of Velox. Center of Symmetry (COS) analysis, which determines the degree of centro-symmetry for each atomic column in the experimental HAADF-STEM image and thus identifies distortions in the stacking sequence, was performed according to the procedure described in [18,53]. The differentiation between extrinsic stacking faults (ESF) and twin stacking is based on the description used in Ref. [68].

2.4. High-resolution digital image correlation

Before deformation, a speckle pattern consisting of 60 nm silver nanoparticles was formed on the surface of the sample, following the procedure developed by Montgomery al. [69]. HR-DIC was performed upon completion of each step using proprietary software, XCorrel [38]. HR-DIC images were captured before loading and after unloading for subsequent analysis. The SEM images (6144 px × 4096 px) were divided into subsets of 31 × 31 pixels (700 nm × 700 nm) with an overlap of 28 pixels between each subset, i.e., step size of 3 pixels (67 nm).

2.5. HR-DIC speckle pattern stability under liquid nitrogen and helium exposure

The assessment of variability in HR-DIC measurements follows the methodology outlined in Ref. [70,71]. This involves the measurement of strain variability using numerous image pairs captured at the same location without any mechanical deformation, as detailed in Sections 2.3 and 2.4. The samples underwent a 30-minute immersion in either liquid nitrogen or liquid helium, followed by a 15-minute

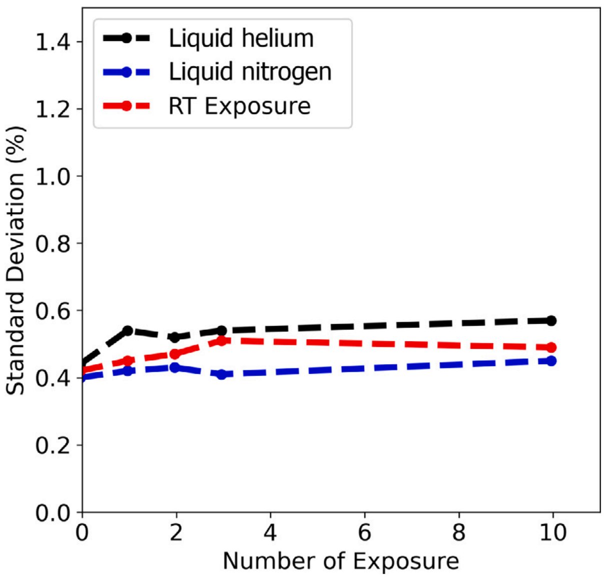

Fig. 2. Stability of the speckle under repeated liquid nitrogen and helium immersion. Average standard deviation on ϵ_{xx} from HR-DIC measurements as a function of the number of immersions in liquid nitrogen and liquid helium.

cleaning in acetone using a sonicator. High-resolution imaging was then performed using an SEM, with conditions described in Section 2.3. Since the specimens were not mechanically deformed, only rigid-body motion should be observable in the kinematics displacement. However, factors such as drift, spatial distortions, and beam scanning defects can introduce errors in HR-DIC measurements, as reported in Ref. [70,72]. Additionally, exposure to liquid helium and nitrogen and the cleaning process could alter the speckle pattern.

The average standard deviation of the ϵ_{xx} strains (in the SEM scanning direction, i.e., horizontal direction) after immersion at different temperatures is presented in Fig. 2. For comparison, the average standard deviation for samples imaged multiple times without immersion in liquid helium or nitrogen and without acetone cleaning is also provided, labeled as "RT Exposure". Minimal variations in standard deviation are observed due to the multiple immersions in liquid helium or nitrogen. Furthermore, the average standard deviation under liquid nitrogen or helium immersion is comparable to that obtained without cryogenic temperature exposure and cleaning, indicating the stability of the speckle pattern even after multiple immersions in liquid nitrogen or helium.

2.6. Heaviside-DIC for deformation twinning and dislocation slip identification

To analyze plastic deformation, the effective strain, ϵ_{eff}, as defined in the Ref. [73,74], is preferred over the ϵ_{xx} strain and will be utilized in subsequent analyses. The effective strain is a term dominated by shear, that better reflects plastic deformation event characteristics. Additionally, the Heaviside-based digital image correlation (Heaviside-DIC) method will be employed to quantitatively characterize the localization of plastic deformation. Heaviside-DIC was developed by multiple research groups to address the issue of discontinuities present within displacement fields [38,75–77]. The Heaviside-DIC method is utilized to extract quantitative measurements of the magnitude of discontinuous displacements, such as displacement induced by crack and slip, across large areas during material deformation. It employs a localized approach that provides additional analysis within the DIC subsets. Discontinuities at the subset level are described by Heaviside functions, enabling one part of the subset to shift in relation to others by an amount equivalent to the physical amplitude of the discontinuities. When mechanical loading occurs, and the dominant mode is dislocation slip, slip traces appear on the free surface of specimens, each associated with a local surface step [78]. In-plane displacements occur within the material between both sides of the slip trace, as illustrated schematically in Fig. 3(a). These displacements can be described by a vector known as the in-plane slip vector $\vec{\tau}$ [38], depicted in red in Fig. 3(a). The in-plane slip vector represents the in-plane displacement caused by a slip event and corresponds to the projection of the cumulated Burgers vector(s) into the specimen surface [38]. The Heaviside-DIC method [38] can quantify the magnitude and direction of the vector $\vec{\tau}$, with the direction described by the angle γ in Fig. 3(a). The angle γ is defined between the slip trace and the in-plane slip vector.

In this study, the Heaviside-DIC technique is updated to enhance the detection and measurement of deformation twinning and closely-spaced slip events. The method involves an additional sub-region within the subsets, as illustrated in Fig. 3(b–c), where a region within the subset, labeled as a "transition region", is considered. This region connects the regions depicted in red and blue in Fig. 3(b–c) by a linear displacement. The correlation is then performed on the entire subset using a Heaviside function to capture the displacement of the regions depicted in red and blue.

The identification of the transition region and the displacement of the red and blue regions in Fig. 3(b–c) is achieved using Newton minimization, a technique common in standard Heaviside-DIC [75]. This approach enables the measurement of the thickness t of the transition region post-deformation, which corresponds physically to the thickness of the deformation event (deformation twin thickness or distance between the furthest spaced slip events) on the surface plane of the specimen. Additionally, it allows for the determination of the in-plane vector, $\vec{\tau}$, which signifies the projection of the cumulated Burgers vector(s) of the Shockley partials (deformation twin) or full (in closely-spaced slip) dislocations onto the specimen's surface.

This refined Heaviside-DIC method enhances the capability to measure the thickness of deformation twins or closely-spaced slip events using HR-DIC data. When the conventional Heaviside-DIC technique is applied to closely-spaced slip events, the in-plane vector $\vec{\tau}$ represents the cumulative displacement of all slip events within the deformation event, as demonstrated in Ref. [79]. However, the conventional Heaviside-DIC method does not provide information about their spacing. By incorporating a transition region in the subset, the modified Heaviside-DIC method can quantify the thickness of closely-spaced slip events, where thickness refers to the distance between the furthest spaced slip events.

2.7. Synthetic images

To assess the measurement accuracy of the updated Heaviside-DIC, synthetic images were generated, as described in Ref. [26], to replicate an experimental speckle pattern, along with a deformation field induced by slip and deformation twinning. Each synthetic speckle was produced using a half cosine function, randomly replicated to form the complete image, with a resolution of 3200 × 3200 pixels. Known deformations were then applied to the initial synthetic image, and the resulting image was created by integrating 10 × 10 pixels to maintain the initial dimensions. This approach was utilized to minimize the impact of interpolation in the deformation process and ensure precise sub-pixel movements.

Two sets of images were created: one set containing four distinct deformation events illustrated schematically in Fig. 4(a); one set containing a deformation event constituting closely-spaced slip as shown in Fig. 4(b). The first set of images includes the following events from left to right: (i) slip event (slip n°1), exhibiting vertical shearing with an amplitude of 3 pixels; (ii) deformation twinning event (twin n°1), displaying a twin thickness of 1 pixel and a vertical displacement of 3 pixels; (iii) deformation twinning event (twin n°2), exhibiting a twin thickness of 2 pixels and a vertical displacement of 3 pixels; (iv)

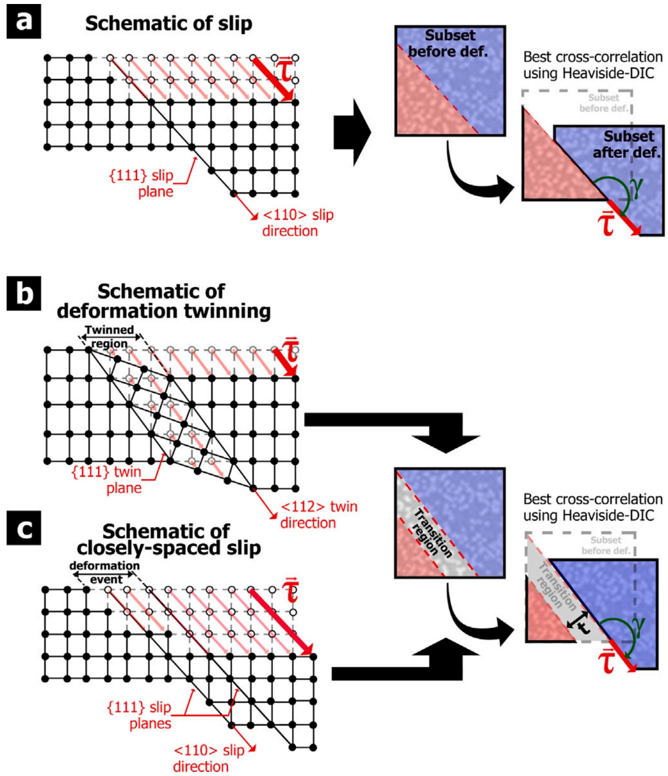

Fig. 3. Displacement induced by slip (a) deformation twinning (b) and multiple closely-spaced slip (c). (a) The Heaviside-DIC provides a theoretical displacement that corresponds to a displacement of one side of the subset along $\vec{\tau}$. The orientation of $\vec{\tau}$ can be described by γ. **(b,c)** When deformation twinning is active, or multiple closely-spaced slip occurs, the updated Heaviside-DIC considers a transition region within the subset that describes the thickness of the overall deformation event. In addition to $\vec{\tau}$ and γ, the thickness t of the deformation event is provided. In the case of twinning, t represents the in-plane thickness of the twin. In the case of closely-spaced slip events, t refers to the distance between the furthest spaced slip events.

deformation twinning event (twin n°3), exhibiting a twin thickness of 3 pixels and a vertical displacement of 3 pixels. The last image set shown in Fig. 4(b) presents a scenario with three closely-spaced slip events. A distance of 2 pixels separates each event and exhibits a vertical displacement of 1 pixel. Additional sets displaying both vertical and horizontal shearing for slip and twin are included in the supplementary material for validation purposes.

3. Results

In the present study, the term "plastic deformation localization" is favored over "plastic strain localization" because the continuum mechanics formulation of strain should not effectively describe the displacements induced by discrete dislocation events that emerge at the surface.

The updated Heaviside-DIC method is initially demonstrated by employing synthetic images generated in Section 2.7. This demonstration is intended to give the reader a better understanding of the associated results obtained. The associated validation of the method is provided in the supplementary material. Subsequently, temperature and microstructure dependencies of slip localization are investigated experimentally using the updated Heaviside-DIC method and STEM characterization from specimens deformed at room, liquid nitrogen, and liquid helium temperatures.

3.1. Demonstration of the updated Heaviside-DIC using synthetic images

Following the methodology outlined, synthetic speckle images were subjected to deformation events of known displacements to simulate the deformation of a material undergoing both slip and deformation twinning. Specifically for set n°1 in Fig. 4(a), the applied displacement induced a vertical step for slip and a constant displacement within the twinned region for deformation twinning along the vertical direction (Y) while producing no displacement along the horizontal direction (X) for all synthetic deformation events. The theoretical displacements for all deformation events along the Y directions are illustrated using transparent gray solid lines in Fig. 5. The results obtained from the DIC calculations on the synthetic images for set n°1 are presented in Fig. 5 for the four synthetic deformation events. Three methods were employed: conventional DIC, Heaviside-DIC constrained to slip (Fig. 3(a)), and Heaviside-DIC incorporating kinematic displacements representative of both slip and deformation twinning (Fig. 3(b)). The obtained displacements along the Y direction are displayed for the different synthetic deformation events in Fig. 5.

The results reveal that the conventional DIC method fails to adequately resolve slip, as previously reported in Ref. [38], and deformation twinning events, as evidenced in Fig. 5 by the presence of large displacement fluctuations near the locations of these events. In contrast, both Heaviside-DIC methods, one constrained to slip and the other incorporating kinematic displacements representative of both slip and deformation twinning, provide accurate displacement measurements for the synthetic slip deformation event. As the thickness of the twinned region increases from twin n°1 to twin n°3, the Heaviside-DIC constrained to slip fails to describe the constant displacement within the twinned region accurately. However, the updated Heaviside-DIC method incorporating the formulation of kinematic displacements representative of both slip and deformation twinning provides displacement measurements with minimal variation from the theoretical values.

Additional sets of images are examined in the supplementary material to assess the accuracy of the methods. The updated Heaviside-DIC method, which incorporates kinematic displacements representing both slip and deformation twinning, yields displacement measurements for slip and twin and thickness measurements for twin that deviate minimally from the theoretical values, with maximum differences for the displacement and thickness of less than 14%.

Ultimately, for each subset, information is obtained as the norm and direction of $\vec{\tau}$ presented in Fig. 3 and the size of the twinned region t. Such information is provided in Fig. 6(a–c) for the synthetic deformation events of set n°1. The obtained γ angles (direction of $\vec{\tau}$) displayed in Fig. 6(b) correspond to the theoretical ones with 8° maximum variation using the updated Heaviside-DIC incorporating kinematic displacements representative of both slip and deformation twinning. Heaviside-DIC incorporating kinematic displacements representing both slip and deformation twinning displays the norm of $\vec{\tau}$ around 3 pixels within 9% maximum variation. The thicknesses of the twinned regions using the Heaviside-DIC incorporating kinematic displacements representing both slip and deformation twinning are displayed in Fig. 6(c) and correspond to the theoretical values with 14% maximum variation. For the synthetic slip event, a thickness of less than 1 pixel approaching a value of 0 is obtained.

An additional set of images to showcase closely-spaced slip is synthetically generated, and the results from the updated Heaviside-DIC method are accessed. The synthetic deformed image can be seen in Fig. 4(b), which illustrates three closely-spaced slip events, each with a shearing of 1 pixel along the Y direction and spaced 2 pixels apart. The in-plane amplitude (magnitude of $\vec{\tau}$), in-plane direction (direction of $\vec{\tau}$), and in-plane thickness (value of t) maps obtained through the updated Heaviside-DIC are shown in Fig. 6(d–f), respectively. Notably, the updated Heaviside-DIC recognizes a single deformation event with a cumulative shear of approximately 3 pixels within 9% maximum variation, an in-plane direction close to 180° within 8° maximum variation, and a thickness t of roughly 4 pixels within 14% maximum variation. Although it does not distinguish individual slip events in closely-spaced

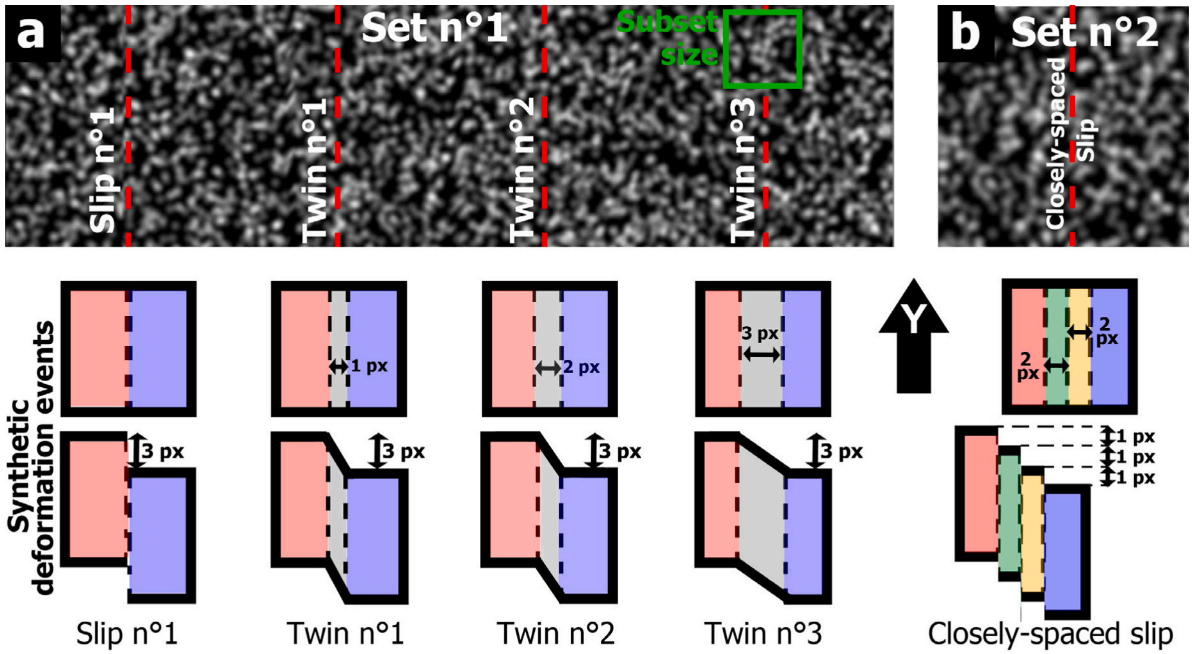

Fig. 4. Synthetic slip and deformation twinning events. (a) Four deformation events, located along the dashed red lines, are included in the synthetic images that mimic displacement induced by a single slip or deformation twinning with shearing along the vertical direction. The applied displacements are schematically described at the bottom. The regions highlighted in red are fixed, while regions highlighted in blue were applied vertical displacements. **(b)** An additional case that consists of three closely-spaced slip events is synthetically generated. (For interpretation of the references to color in this figure legend, the reader is referred to the web version of this article.)

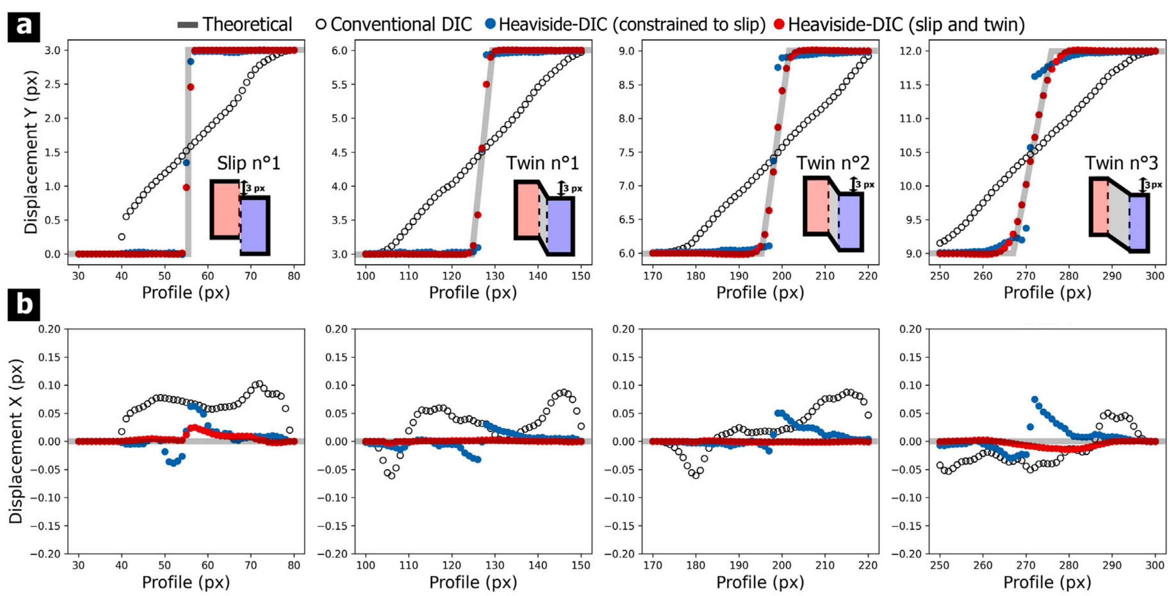

Fig. 5. Heaviside-DIC on synthetic slip and deformation twinning events. Vertical displacements across slip **(a)** and deformation twinning events **(b,c, and d)** using conventional DIC, Heaviside-DIC constrained to slip, and updated Heaviside-DIC incorporating kinematic displacements representative of both slip and deformation twinning. Schematics of the synthetic deformation events are presented in insets. Twin thicknesses are 1 pixel **(b)**, 2 pixels **(c)** and 3 pixels **(d)**. The transparent gray solid lines indicate the theoretical applied displacements.

slip deformations, the updated method yields a thickness that describes the distance between the outermost slip events. The updated method allows quantifying closely-spaced slip events from individual ones. However, without more information, it remains impossible to differentiate closely-spaced slip from deformation twinning.

In conclusion, when using the experimental parameters employed, the updated methodology exhibits a sensitivity for displacement detection equivalent to 9 nm, mirroring the performance of the traditional Heaviside-DIC method as reported in Ref. [38]. This indicates that the method is adept at identifying displacements with resolutions exceeding 9 nm. Moreover, the revised approach successfully differentiates between twinning and single slip for thicknesses greater than 22.4 nm. The precision in measuring thickness and displacement amplitude is noted to be approximately 9 nm and 6 nm, respectively.

3.2. Temperature dependence of plastic deformation localization

The updated method is now used to investigate plastic deformation localization at room and cryogenic temperatures in the investigated

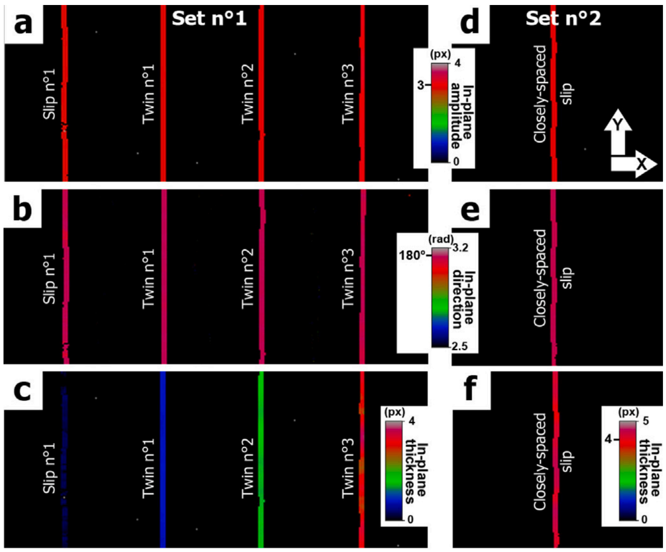

Fig. 6. In-plane amplitude **(a)**, in-plane direction **(b)** and in-plane thickness **(c)** maps obtained from the updated Heaviside-DIC method for the considered synthetic deformation events in set n°1 (a,b,c) and set n°2 (d,e,f).

nickel-based superalloy. Plastic deformation localization is referring in the present article as the intensity of surface deformation induced by plasticity (slip and planar defects). The ϵ_{eff} strain maps obtained after deformation at room, liquid nitrogen, and liquid helium temperatures are displayed in Fig. 7(a,d, and f), respectively. The applied macroscopic plastic strains are 1.22%, 0.83%, and 0.88%, respectively. The ϵ_{eff} strain map for a reduced region of interest is provided in Fig. 7(b) for the specimen deformed at room temperature. In-plane amplitude maps of reduced regions of interest are shown in Fig. 7(c,e, and g) for the specimens deformed at room, liquid nitrogen, and liquid helium temperatures, respectively. These maps display the in-plane displacements, in nanometers, induced by the deformation events. The associated inverse pole figure map along the loading direction for the specimen deformed at room temperature is provided in the inset in Fig. 7(a). For each of the three temperatures studied, we investigated a region measuring 1076x1030 μm^2, which includes approximately 800 crystallographic grains with about 45% of the grain boundaries being annealing twin boundaries. The analysis covered 1266 deformation events to ensure a representative analysis.

Maps obtained at room or cryogenic temperatures appear similar, with multiple intense plastic deformation localization events per grain, evidenced by concentrated strain bands. Even within the cryogenic temperature range, the strain maps do not show any noticeable differences, as can be observed by comparing the maps obtained at liquid nitrogen and liquid helium temperatures in Fig. 7(d and f). This is despite the fact that the macroscopic tensile behavior at liquid helium temperature is significantly different from that at liquid nitrogen temperature, as is evident from the serrated yielding phenomenon observed at liquid helium temperature in Fig. 1(d). The updated Heaviside-DIC approach is used to characterize the nature of the plastic deformation localization events statistically. For each plastic deformation localization event, the maximum in-plane amplitude and average thickness were extracted from the measurements performed at room temperature, liquid nitrogen, and liquid helium temperatures. The in-plane amplitude and average thickness distributions of the investigated events are represented in Fig. 8(a and b), respectively, as a function of applied macroscopic plastic strain and temperature at which the specimens were tested.

On average, it is noticed that the maximum in-plane amplitude increases as the temperature decreases and macroscopic plastic strain increases. Moreover, when the temperature drops to cryogenic levels, most of the plastic deformation localization events exhibit in-plane thicknesses greater than 1 pixel (22.4 nm), suggesting deformation events involving either deformation twinning or closely-spaced slips. In contrast, more than 95% of the deformation events occurring at room temperature display an in-plane thickness lower than 1 pixel (22.4 nm).

The average in-plane direction per plastic deformation event as previously defined in Section 2.6 and in Ref. [38] is used and described by the angle γ as shown in Fig. 3. For each plastic deformation localization event, the average experimental in-plane direction is compared with the three theoretical, obtained from EBSD measurements, projected <110> and <112> in-plane directions (which are projections of <110> and <112> onto the surface plane) within the experimentally observed {111} active plane. The minimum difference (angle) between the experimental and theoretical directions for the <110> and <112> in-plane directions are selected and displayed in Fig. 9 for specimens deformed at room, liquid nitrogen, and liquid helium temperatures. Each point corresponds to a deformation event, and heat maps are created to identify areas of concentration. In Fig. 9, a positive angular difference indicates that the experimentally obtained γ angle is larger than the theoretical one, while a negative angular difference indicates the converse.

In Fig. 9(a), which displays deformation event characteristics for the specimen deformed at room temperature at a macroscopic plastic deformation of 1.22%, it is unsurprisingly observed that there is a concentration of points along the plot's vertical direction, indicating minimal variation between experimental values and the theoretical <110> slip direction. Similar concentration along the vertical direction is also observed, to a lesser extent, for plastic deformation localization events occurring at cryogenic temperatures, as shown in Fig. 9(b,c, and d) for low levels of applied plastic deformation, with most of the events closely aligned with a theoretical <110> slip direction. With increasing applied plastic strain at liquid nitrogen temperature from 0.65% to 3.86% (Fig. 9(b,d,e, and f)), the distribution changes from a concentration of points along the plot's vertical direction to a concentration along the plot's horizontal direction as observed in Fig. 9(f) for an applied plastic deformation of 3.86%. Similarly, a concentration of points along the plot's horizontal direction, indicating shearing along <112>, is observed for the specimen deformed at liquid helium temperature for a relatively low plastic deformation of 0.99% as observed in Fig. 9(g).

The absolute deviation from <110>, discussed in Fig. 9 and the preceding paragraph, for deformation events at macroscopic plastic deformations of 0.65% and 3.86% at liquid nitrogen temperature, is presented in Fig. 10. The Y-axis of this figure displays the intensity of the investigated events. To enhance visualization, Fig. 10 reports the absolute values (always positive) of the deviation from <110>.

The observations from Fig. 10 indicate that for the specimen deformed at liquid nitrogen temperature, deformation events with significant deviation from the <110> direction show low in-plane amplitude at an applied plastic deformation of 0.65%. This phenomenon is not evident in the specimen deformed at the same temperature but with a higher applied plastic deformation of 3.86%.

The previous plots in Fig. 9(b and c) and in Fig. 8(b) indicate that the large majority of plastic deformation localization events occurring during deformation at low level of applied plastic strain at cryogenic temperatures display: (i) an average shearing along a <110> direction; (ii) a significant in-plane thickness. It is also observed in Fig. 11(b and c) from the high-resolution SEM images, used for HR-DIC, of the specimen surfaces after deformation at liquid nitrogen and helium temperatures, respectively, that closely-spaced slip steps are occurring. This characteristic is highly pronounced at liquid helium temperature, where numerous closely-spaced slips occur at certain locations, as illustrated in the inset of Fig. 11(c). Conversely, most of the plastic deformation localization events observed at room temperature deformation seem (within the available resolution of the images and HR-DIC)

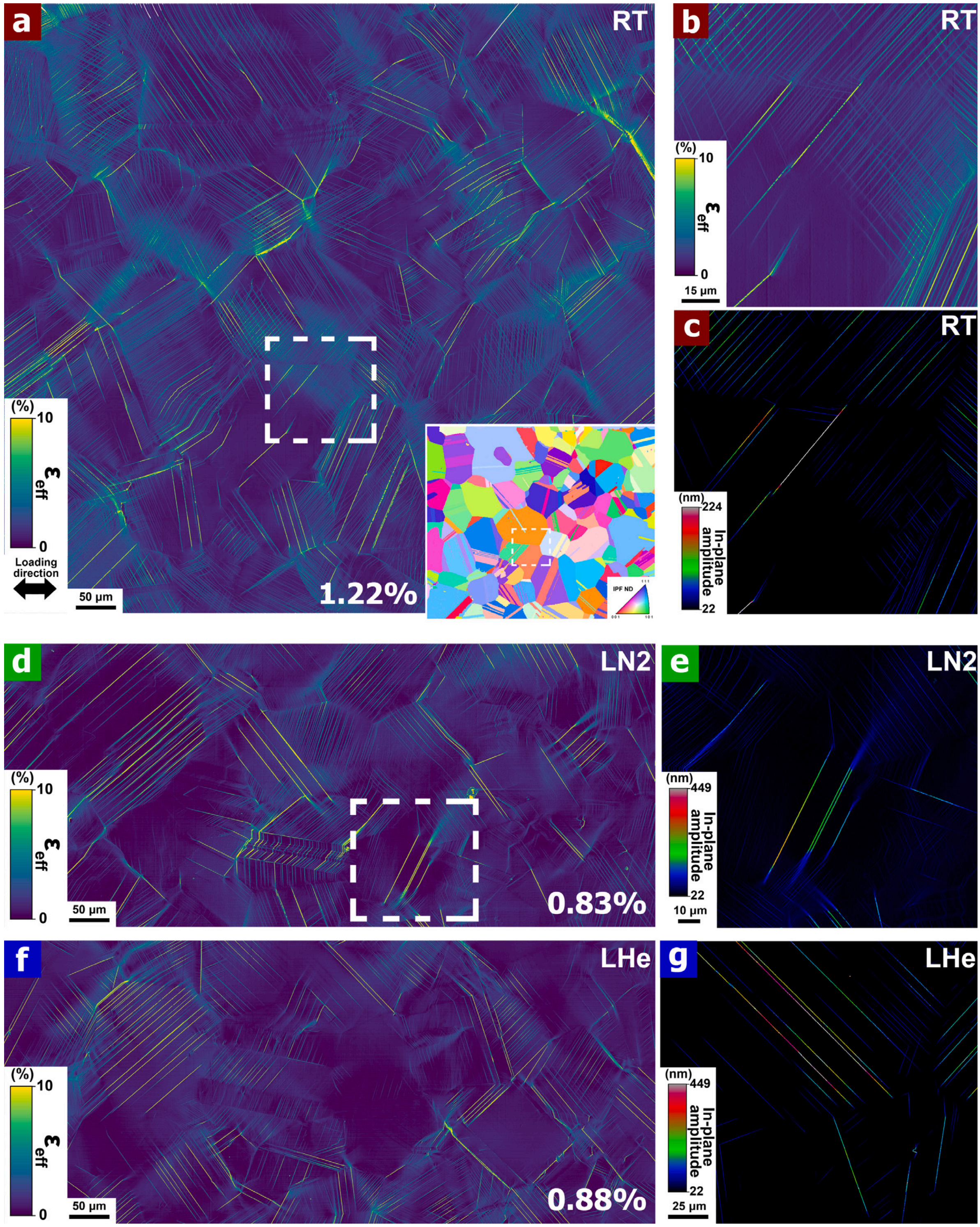

Fig. 7. Strain maps ϵ_{eff} showing plastic deformation localization at room **(a,b)**, liquid nitrogen **(d)** and liquid helium **(f)** temperatures after 1.22%, 0.83% and 0.88% plastic deformation, respectively. Associated in-plane amplitude maps for a reduced region of interest for specimens deformed at room **(c)**, liquid nitrogen **(e)**, and liquid helium temperatures **(g)**. The inset in **(a)** displays the associated inverse pole figure map for the specimen deformed at room temperature. For clarity, only a subset of the investigated region is displayed for the specimens tested at liquid nitrogen and helium temperatures.

to comprise a single slip step, as shown in Fig. 11(a). The occurrence of closely-spaced slip steps over extended regions is even more visible for a specimen deformed at 1.86% at liquid helium temperature as shown in Fig. 11(d and e).

To further investigate the occurrence of an increasing number of closely spaced events within deformation events at cryogenic temperatures, numerous cross-sections transverse to deformation events were extracted using TEM surface lamella preparation by FIB at different temperatures. It was systematically observed that the number of slip steps increased with decreasing temperature, as shown in Fig. 12.

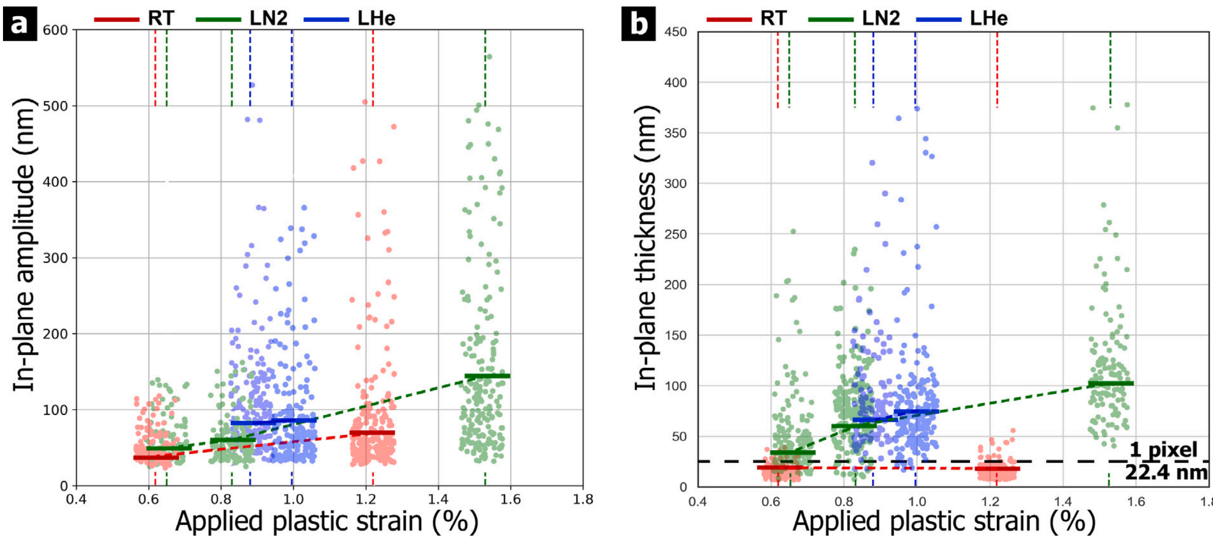

Fig. 8. (a) Distribution of the in-plane amplitude for specimens tested at room, liquid nitrogen, and liquid helium temperatures as a function of the applied macroscopic plastic strain. Each dot corresponds to a deformation event, i.e., concentrated strain bands in Fig. 7. **(b)** Distribution of the in-plane thickness for specimens tested at room, liquid nitrogen, and liquid helium temperatures as a function of the applied macroscopic plastic strain. The horizontal bars display the average of the distributions. The data is slightly spread out along the *x*-axis for each applied macroscopic plastic strain to improve the graph's readability.

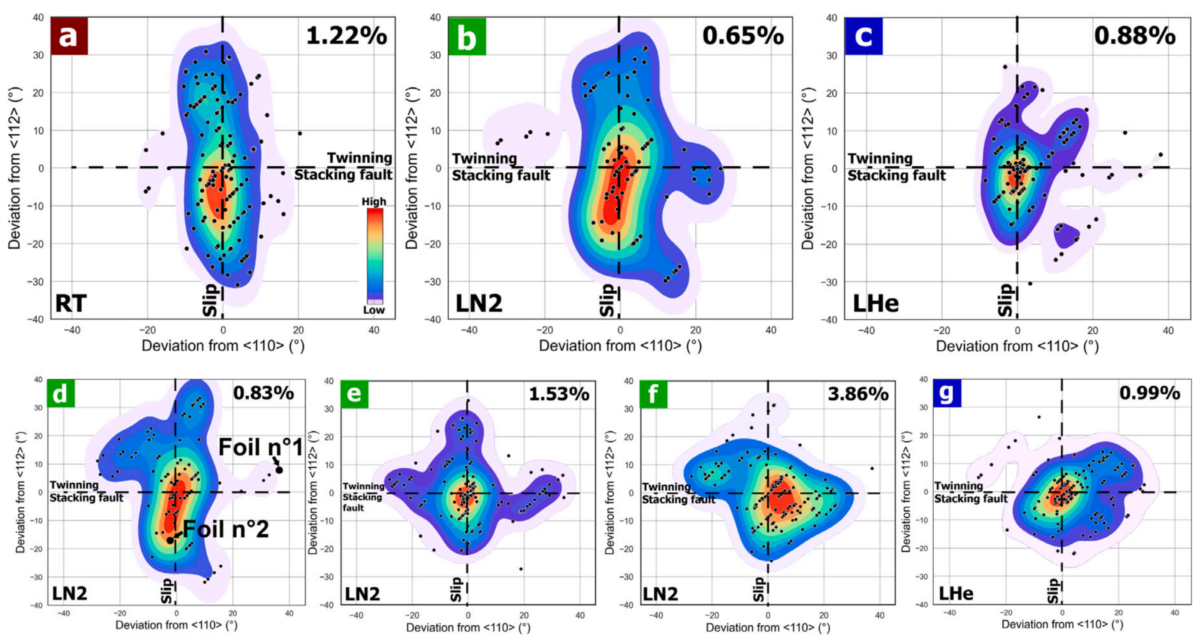

Fig. 9. Distributions and contour plots of the minimum differences expressed in degrees between the experimental value of the in-plane direction obtained from Heaviside-DIC and the three theoretical <110> and <112> in-plane directions from EBSD measurement (which are projections of <110> and <112> onto the surface plane) within the experimentally observed {111} active plane. **(a)** Room temperature deformation at 1.22% macroscopic plastic strain. **(b,d,e and f)** Liquid nitrogen temperature deformation at 0.65%, 0.83%, 1.53% and 3.86% macroscopic plastic strain, respectively. **(c and g)** Liquid helium temperature deformation at 0.88% and 0.99% macroscopic plastic strain.

At room temperature, deformation events typically involved one (see Fig. 12(a)) or, in rare cases, two steps, whereas multiple steps per deformation event were present at cryogenic temperatures (see Fig. 12(b,c)). Notably, isolated planar defects were observed in the lamellae extracted from deformation events at liquid helium temperature, as indicated by the green arrow in Fig. 12(b).

To investigate the deformation mechanisms at cryogenic temperatures and their relation to the observed increased thickness of the plastic deformation events, STEM observations were conducted on deformation events highlighted in Fig. 13 that displayed average thicknesses of 201 nm and 45 nm, respectively. The STEM analysis focuses on the events marked as "Foil n°1" and "Foil n°2" in Fig. 13, with events in Foil n°1 displaying large deviation from <110> and events in Foil n°2 displaying no deviation from <110>. The slip events that are being explored with these foils are indicated in Fig. 9(d).

The BF-STEM DCI overview of Foil n°1, Fig. 14(a), reveals three distinct plastic deformation events, as also observed in the strain map of Fig. 13. Each event is observed to produce a significant extrusion at the surface and thickness, coherent with the significant value of the in-plane amplitude observed in Fig. 13(b). The events occur parallel and slightly offset from annealing twin boundaries (ATBs) that were present before deformation. Intense deformation events were often observed near and offset from ATBs similarly to previous observations at room temperature [80]. Interestingly, the deformation events reveal distinct diffraction contrasts associated with the presence of dislocations, as illustrated in Fig. 14(b and d), and deformation twins, as seen in Fig. 14(c

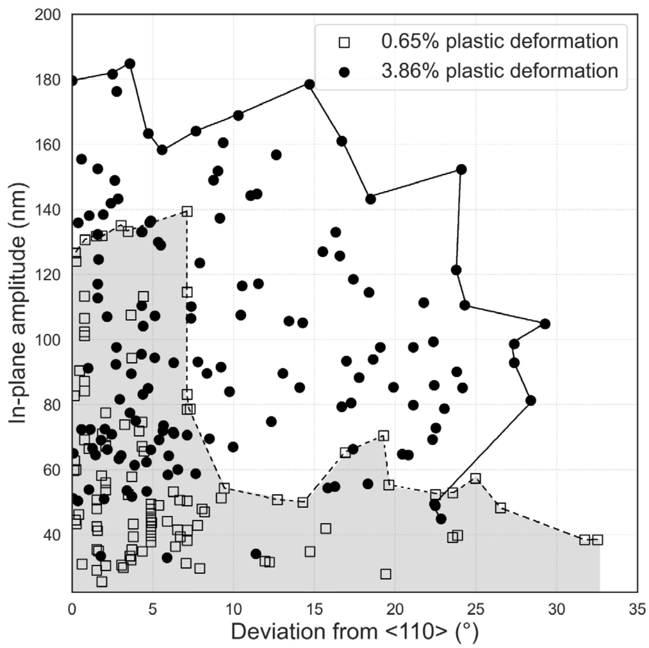

Fig. 10. Distributions of the in-plane amplitude as a function of the minimum differences expressed in degrees between the experimental in-plane direction obtained from Heaviside-DIC and the three theoretical <110> in-plane directions (which are projections of <110> onto the surface plane) obtained from EBSD within the experimentally observed {111} active plane. Absolute values of the difference were considered for better visualization in contrast to the plots in Fig. 9(b and f). Specimens were deformed at liquid nitrogen temperatures at macroscopic plastic deformation of 0.65% and 3.86%.

and e). Additionally, both intrinsic (ISF) and extrinsic (ESF) stacking faults are evident in Fig. 14(f). Notably, these events are predominantly deformation twinning, with twins with thicknesses ranging from a few nanometers up to more than 20 nm.

In contrast, Foil n°2 exhibits deformation events primarily driven by dislocations, as depicted in detail in Fig. 15(b). The atomic-resolution HAADF-STEM image in Fig. 15(c) and corresponding COS map in Fig. 15(d) also reveal a range of defects, including ISF, ESF, nano-twins, twin embryos, and even short, truncated "lens-shaped" hexagonal-close packed (HCP) regions. Unlike Foil n°1, Foil n°2 features twins that extend no more than a few atomic layers. As described in detail in Ref. [81], these features are consistent with movement of individual and groups of 1/2<110> dislocations, and their interaction with the γ' and γ'' precipitate structures.

3.3. Temperature dependence of microstructure effects

The spatial correlation between EBSD and HR-DIC measurements, as outlined in Section 2.3, facilitates the understanding of microstructural effects on plastic deformation localization. From the tests conducted at room temperature, liquid nitrogen temperature, and liquid helium temperature, with applied plastic strains of 1.22%, 0.83%, and 0.99%, respectively, the 10% most intense plastic deformation localization events (characterized by the highest maximum in-plane amplitude) were identified. The most intense localization events were found to exhibit a parallel slip configuration [82]. This configuration refers to deformation events occurring parallel to and near a coherent annealing twin boundary, as illustrated in Fig. 16(a). Out of the 10% most intense plastic deformation localization events extracted from specimens at the investigated temperatures, 95% from room temperature, 91% from liquid nitrogen, and 91% from liquid helium were linked to a parallel slip configuration. Conversely, 5% from room temperature and 9% of them from both liquid nitrogen and liquid helium temperatures were associated with intragranular events, i.e., they occurred within the grain and not near and parallel to an annealing twin boundary.

Moreover, twin boundaries that exhibit the highest plastic deformation localization events are noted for their extended lengths (not presented here). The distribution of the directional misorientation (along the loading direction) across twin boundaries, which show the highest plastic deformation localization, is presented in Fig. 16(c) for specimens deformed at room temperature, as well as at liquid nitrogen and helium temperatures. Consistent with findings from previous studies [82], these twin boundaries, after deformation at room temperature, are identified by a wide range of directional misorientations, with large directional misorientation maximizing the mismatch in directional elastic modulus and presenting a low Schmid factor for the <110> slip directions. Similar observations are made for specimens tested at liquid nitrogen and helium temperatures, where twin boundaries with large directional misorientation activate intense plastic deformation events. It is also noted that a significant number of intense deformation events are also occurring near and parallel to twin boundaries that display low directional misorientation across the twin boundary. When the directional misorientation is low, the configuration, by geometric consideration, presents a high Schmid factor for the <110> slip directions [82].

4. Discussion

4.1. Heaviside-DIC method for deformation twinning and slip characterization

At room temperature, slip is the primary deformation mechanism in FCC materials. However, under specific conditions such as cryogenic temperature loading, deformation twinning can emerge as the predominant mechanism. Distinguishing between these two mechanisms is crucial because they significantly influence the mechanical properties of materials. Their competitive nature often complicates the identification of their individual contributions. While TEM is invaluable for this purpose, it lacks the ability to facilitate statistical analysis. Traditional HR-DIC measurements offer statistical insights but fall short of providing quantitative data on the contributions of slip and twinning.

The updated Heaviside-DIC method introduced and validated in this paper, incorporating the physical displacement at the subset scale to describe both slip and twinning, offers a precise depiction of these events. Nonetheless, it is important to acknowledge certain limitations of this method. Firstly, the approach's exclusion of regions within subsets to represent twinned regions means that twins thinner than 1 pixel (22.4 nm, based on the experimental parameters of this study) cannot be distinctly identified from slip. This issue arises because a region smaller than 1 pixel cannot be considered within a subset. However, while the sensitivity for in-plane thickness is at the pixel (22.4 nm), the resolution for in-plane thickness and amplitude achieves sub-pixel accuracy. Secondly, the method cannot differentiate between deformation twinning and closely-spaced slip events, as illustrated in Fig. 6. When multiple slips occur closely within a subset, the observed displacement is the cumulative result of each slip, and the method estimates a thickness that reflects the distance between the furthest slip events. However, when used alongside EBSD measurements, the updated Heaviside-DIC method proves to be a reliable tool for statistically distinguishing between slip and twin deformation events.

The approach of using HR-DIC to differentiate between slip and deformation twinning extended on the in-plane shearing direction has been successfully employed in several studies [25,39,83–85]. However, a deformation event captured by HR-DIC might consist of closely-spaced slip bands, multiple nanometer-scale deformation twins, or a combination of slip and twin [86]. This becomes particularly pertinent when considering deformation at cryogenic temperatures, where competing deformation mechanisms may occur [17]. Due to HR-DIC's

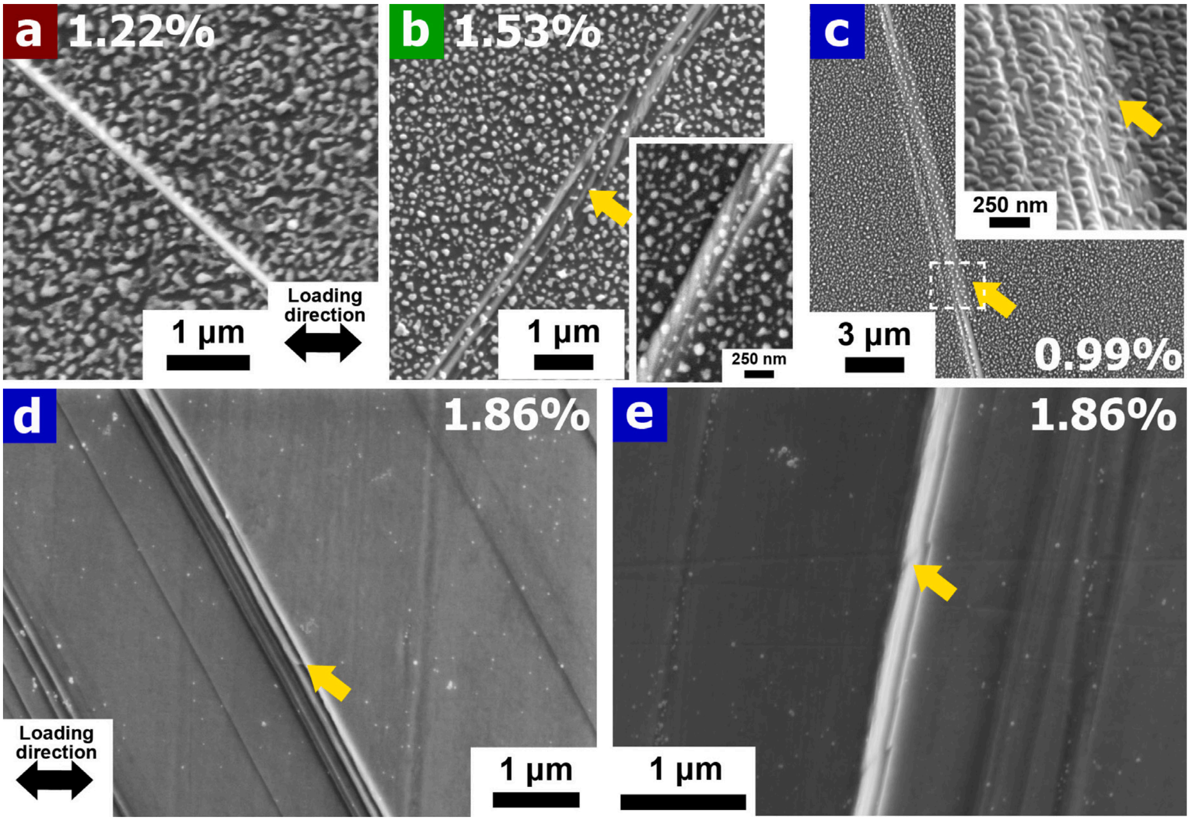

Fig. 11. High-resolution SEM images of intense deformation events as a function of temperature. Surface steps after deformation at room **(a)**, liquid nitrogen **(b)** and liquid helium temperature **(c)**. The visible nanoscale particles form the speckle pattern employed for HR-DIC. The values in white indicate the applied macroscopic plastic strain. **(d,e)** Surface steps after plastic deformation of 1.86% at liquid helium temperature. The speckle pattern was removed for better visualization.

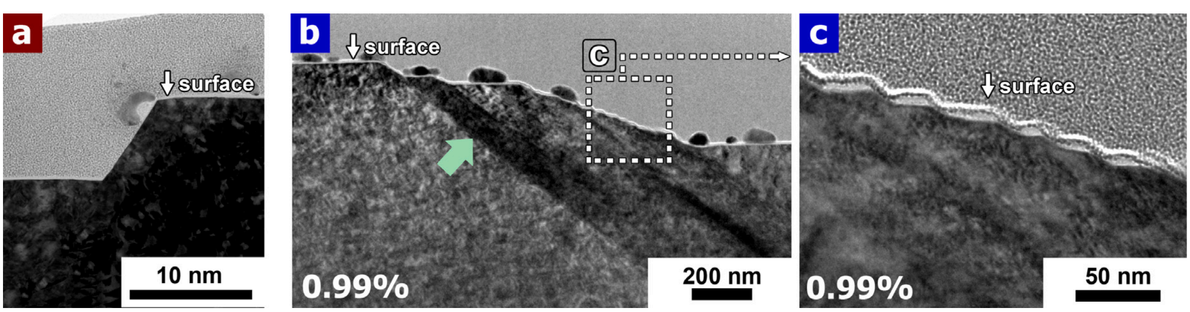

Fig. 12. Surface extrusion as a function of temperature. TEM images of cross-sections across (transverse to) deformation events after deformation at room **(a)**, and liquid helium temperature **(b,c)**. The deformation event in (b) and (c) corresponds to surface steps in Fig. 11(c) and shows the presence of dislocations and planar defects (green arrow). (For interpretation of the references to color in this figure legend, the reader is referred to the web version of this article.)

significantly lower resolution compared to the atomic scale of discrete dislocations and planar defects, it is unreasonable to attempt to identify discrete defects. Nonetheless, the accumulated shearing direction along a deformation event, as identified by HR-DIC, can indicate the dominant deformation processes within this event, as demonstrated in Fig. 9(d) and corroborated by STEM analysis in Figs. 14 and 15. Coupled with the potential for statistical analysis, HR-DIC measurements become valuable for identifying dominant deformation mechanisms. Additionally, HR-DIC measurements can ascertain another critical aspect—the thickness of deformation events, which aids in further identifying the involved deformation mechanisms.

4.2. Slip delocalization at cryogenic temperatures

The STEM results indicate unsurprising activation of deformation twinning at liquid nitrogen and helium temperatures. Twinning was previously reported in the literature for several nickel-based superalloys and used to explain their exceptionally superior cryogenic mechanical properties [7–10] including improvement of fatigue ratio (fatigue strength divided by yield strength) for a nickel-based superalloy 718 at cryogenic temperatures [6]. The present study also identifies deformation twinning as dominant during deformation at cryogenic temperatures for high levels of deformation, as shown in Fig. 9(f and g). However, it is observed that plastic deformation localization is mainly dominated at low levels of applied plastic deformation by deformation events producing shearing along a <110> direction, indicating slip-dominated behavior. Surprisingly, the HR-DIC results indicate a thickness of the deformation events when reaching cryogenic temperatures. The presence of a thickness and overall shearing along a <110> direction indicates the existence of closely-spaced slip within the plastic deformation localization events. It is confirmed by images of the surface step and corresponding STEM analysis as shown in Figs. 11 and 15.

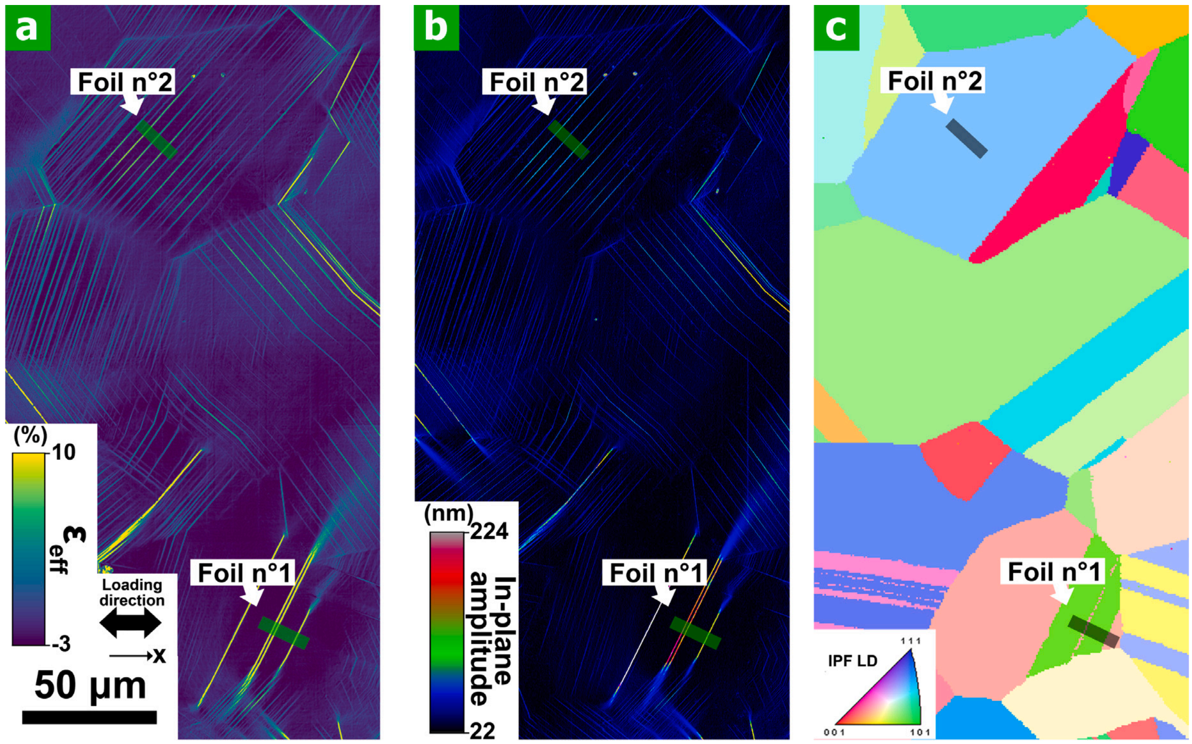

Fig. 13. **(a)** Strain map ϵ_{eff} showing plastic deformation localization at deformation at liquid nitrogen temperature for an applied plastic deformation of 0.83%. **(b)** Associated in-plane amplitude indicating the amplitude of the shearing induced by plastic deformation events. **(c)** Associated inverse pole figure map along the loading direction, measured by EBSD prior to deformation.

During deformation at cryogenic temperatures, plastic deformation is predominantly facilitated by events characterized by closely-spaced slip, a feature that is uncommon in room-temperature deformation. This phenomenon of closely-spaced slip can be described as a plastic/slip deformation delocalization mechanism, where plasticity spreads locally across an extended region. Interestingly, this phenomenon is dominating at a low level of applied plastic strain. At high levels of applied plastic strain, the dominant deformation events are observed to have an in-plane direction aligning with the <112> direction, indicating behavior predominantly governed by deformation twinning. This distinction is also noticeable, albeit to a lesser extent, at relatively low applied plastic strains when transitioning from liquid nitrogen to liquid helium temperatures, as illustrated in Fig. 9(c and g). Interestingly, a significant fraction of deformation events that occur at liquid nitrogen or liquid helium temperatures displays average in-plane displacement corresponding to an intermediate direction between <110> and <112>, indicating the contribution of both slip and non-slip deformation and a domain where competition between slip and deformation twinning is significant.

Additionally, under low levels of deformation at liquid nitrogen temperatures, intense plastic deformation localization events are associated with slip, as shown in Fig. 10. Deformation events showing significant deviation from theoretical shearing along a <110> direction exhibit low in-plane amplitude, as also illustrated in Fig. 10. This confirms that at these low deformation levels, the activation of deformation twinning is not predominant. More importantly, Figs. 10 and 9 show that the deformation events that developed at low levels of deformation evolve during increasing deformation, transitioning from closely-spaced slip to deformation twinning-dominated events.

Three deformation mechanisms could be the origin of the observed slip delocalization process. First, various defects at a small scale, including nano-twins, stacking faults, and HCP regions as observed in Figs. 15 and 12(b) for a deformation event dominated by slip, can mitigate the glide of full dislocations along a single slip plane and reduce planar slip. As such, deformation twin boundaries play dual roles in acting as both barriers to the motion of dislocations and pathways to facilitate the glide of dislocations along twin boundaries. Therefore, the presence of planar defects along a slip band may facilitate the activation of additional slip bands close to the initial slip band. Deformation twins have been observed to be the preferential sites in FCC materials for activation of slip near and parallel to their twin boundary [18]. Moreover, specifically for the 718, a mechanism for the formation of extrinsic faults is proposed involving the cross-slip and a 1/2<110> dislocation [81]. Such processes could lead to numerous narrow and truncated ("lens-shaped") twinned regions as shown in Fig. 15 that could facilitate the observed plastic delocalization. Second, cross-slip may provide a deformation process that induces the slip delocalization mechanism observed at cryogenic temperatures. Massive cross-slip of full dislocations has been previously reported in other FCC materials such as the CrCoNi and CrMnFeCoNi at liquid nitrogen temperatures [17]. Wavy slip was observed along a few deformation events for specimens tested at cryogenic temperatures as shown in Fig. 17(a) and suggests the occurrence of cross-slip. Similarly, slip steps associated with secondary slip systems are noted in the closely-spaced slip events, as indicated by arrows in Fig. 11. Such a process was elegantly explained by Ding et al. [17] in considering that the activation of a specific type of extended defects (partial and full dislocations and deformation twinning) is controlled by mechanical stresses and thermal fluctuations. Because of the reduced intensity of thermal fluctuations at cryogenic temperature, the applied stress has to be elevated to lower the activation energy. Therefore, when the applied stress increases, the activation energies for partial dislocations, full dislocations, and twins are all reduced, such that their differences become much smaller. As a result, nucleation frequency becomes closer for the different types of extended defects [17]. Consequently, the concurrent operation of multiple defect mechanisms at cryogenic temperatures may have a significant influence on the localization of the plasticity by activating

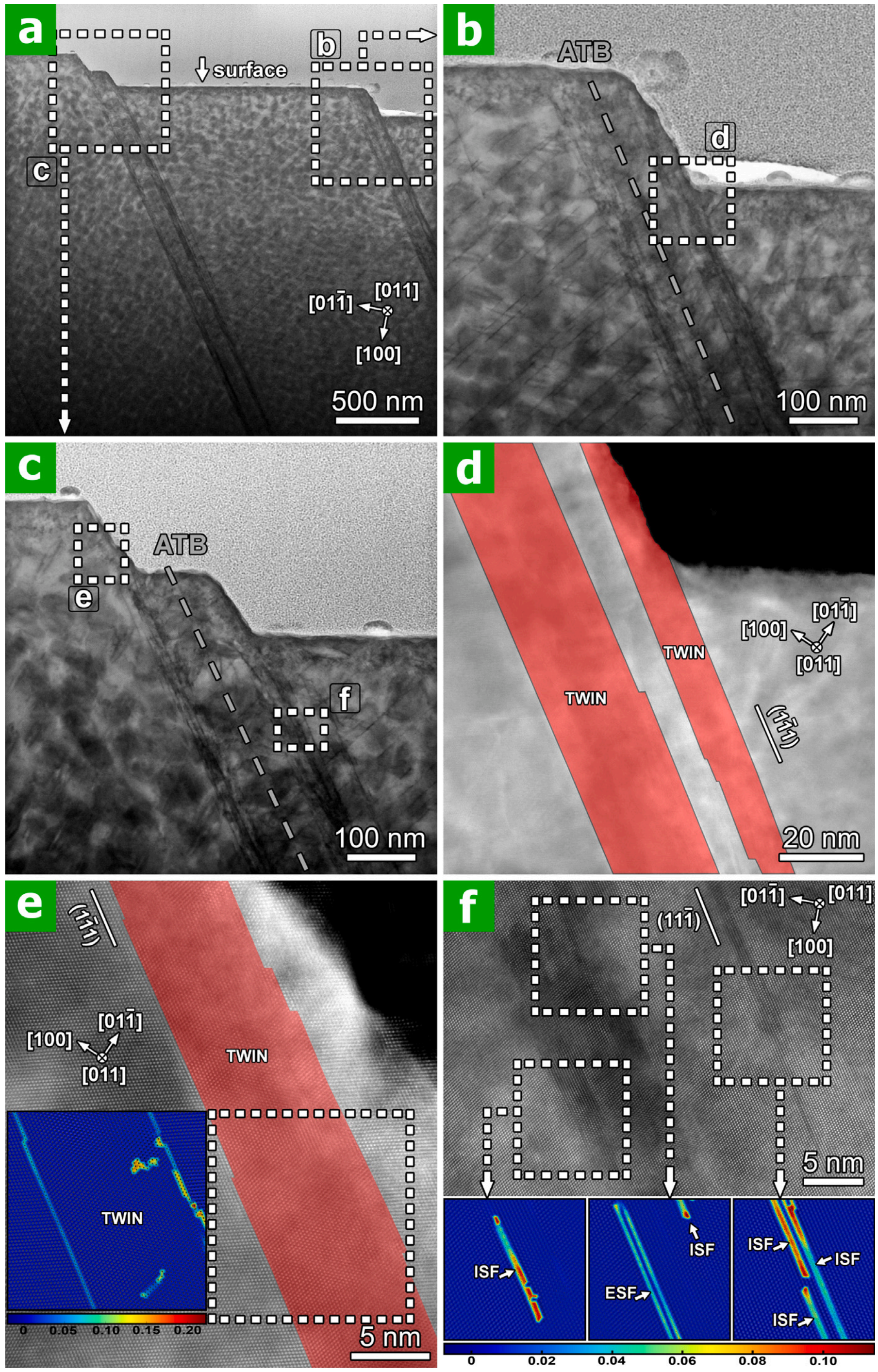

Fig. 14. **(a)** BF STEM-DCI overview of the Foil n°1 showing surface relief and the underlying microstructure. Two locations associated with the steps on the surface are highlighted by white dashed rectangles. **(b)** Detail of "single surface step", and **(c)** detail of "double surface step". The gray dashed lines designate the locations of ATBs. **(d)** HAADF-STEM detail from the edge of the step reveals the presence of two deformation twins. **(e)** HAADF-STEM detail from the edge of the "upper step" and corresponding COS map confirm the presence of deformation twins. **(f)** HAADF-STEM from the band of localized plastic deformation, COS maps confirm the presence of numerous ISFs and ESF.

the observed slip delocalization mechanism. It might seem counterintuitive, considering our knowledge that lower stacking fault energy typically favors planar slip [87]. Third, the development of intense plastic deformation localization events leads to significant stress concentrations at the grain boundary due to slip impingement [80]. This occurs when slip transmission is not favored, resulting in significant dislocation pile-up and ultimately the physical shearing of the grain boundary at the point of plastic deformation impingement. This local shearing induces significant stress redistribution, which can trigger additional slip [43,88]. This phenomenon could trigger the activation of additional slips near the initial one. Such closely-spaced slip events were infrequently observed after deformation at room temperature, as depicted in Fig. 17(b), and further shown by a limited number of deformation events that exhibit thicknesses at room temperature in Fig. 8(b). As the applied stress increases at cryogenic temperatures, the stress concentration resulting from slip impingement may

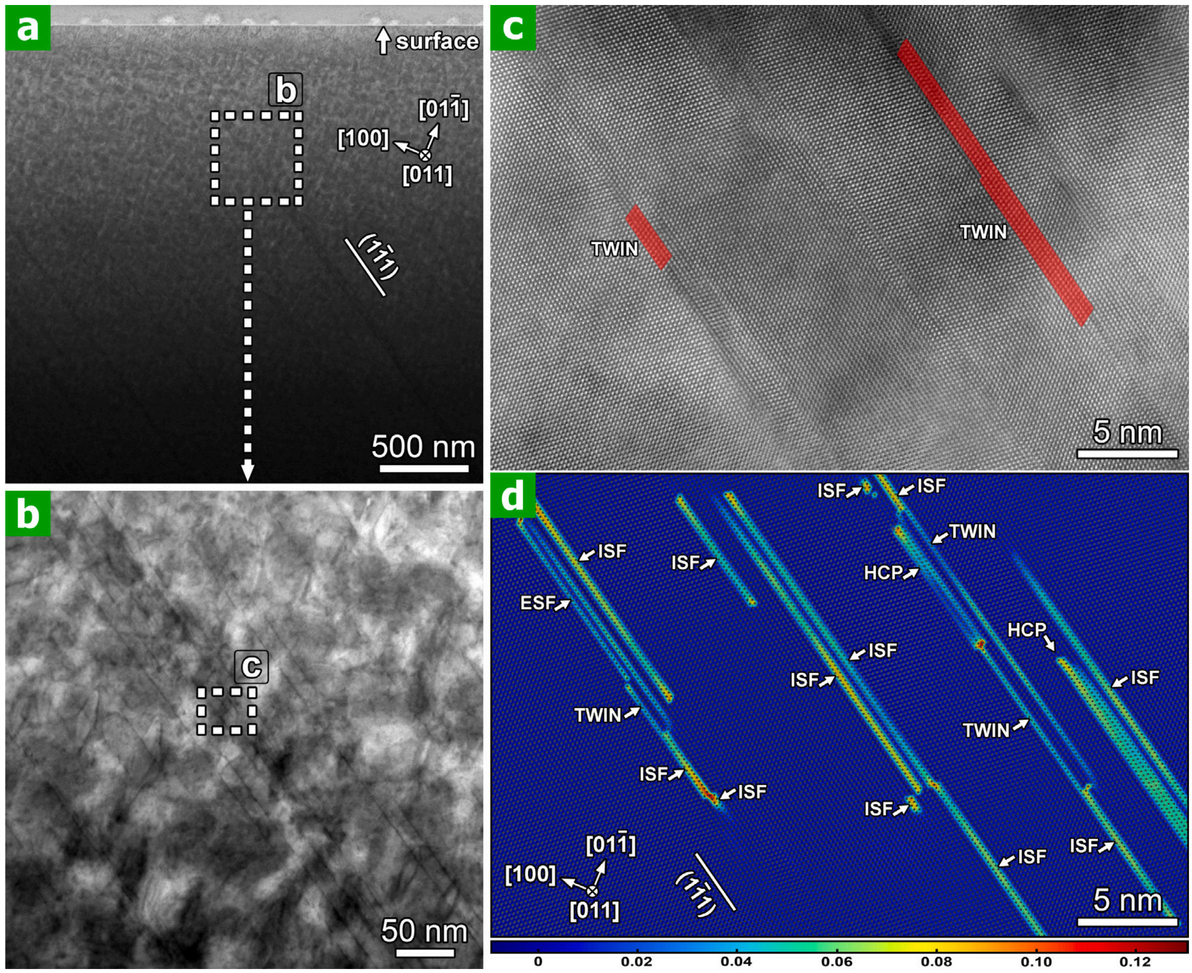

Fig. 15. **(a)** BF STEM-DCI overview of the Foil n°2 showing surface relief with no visible steps, and the underlying microstructure. The electron beam is parallel with the [011] crystallographic zone axis. The area of a localized band of plastic deformation inspected in detail is highlighted by a white dashed rectangle. **(b)** Detail showing several planar slip traces as observed edge-on in the band of localized plastic deformation. **(c)** Atomic resolution HAADF-STEM of the defects from the area highlighted by a white dashed rectangle in **(b)**. **(d)** Corresponding COS map reveals that the band consists of numerous extended ISFs, ESFs, twins, and even HCP bands. These features are consistent with dissociated 1/2<110> dislocations, and subsequent interaction of dislocations with these faults, leading to multi-layered configurations. Thick deformation twins are not observed, in contrast to those seen in Fig. 14.

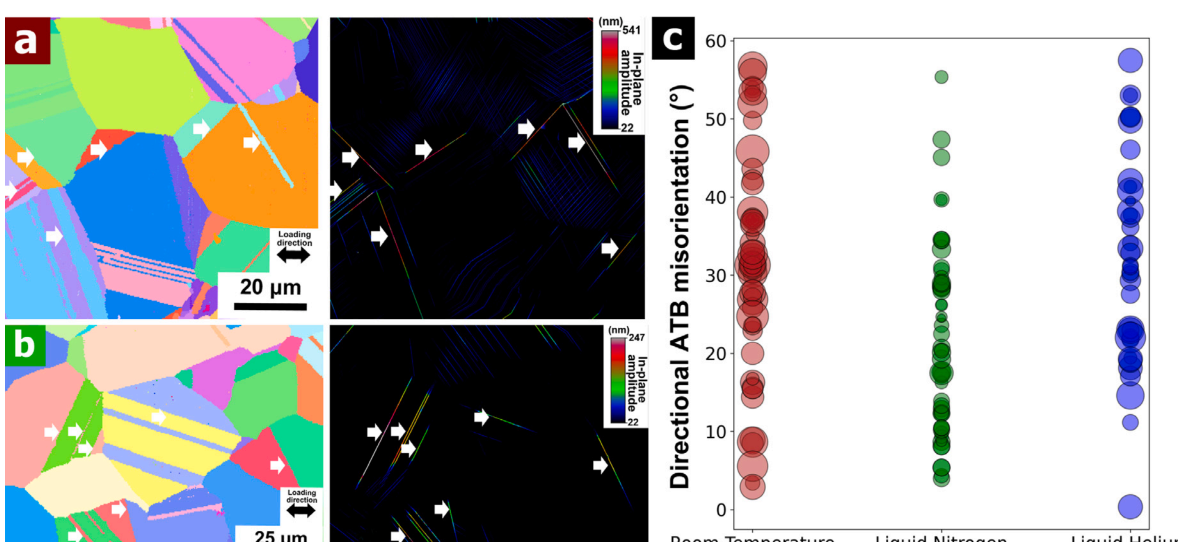

Fig. 16. Intense plastic deformation localization events observed for specimens tested at room **(a)** and liquid nitrogen temperature **(b)** after macroscopic plastic deformation of 1.22% and 0.83% respectively. **(c)** The distribution of directional (along the loading direction) misorientation across twin boundaries for the most intense events observed in parallel slip configuration at room temperature, liquid nitrogen, and helium temperatures after macroscopic plastic deformation of 1.22%, 0.83%, and 0.99% respectively. The size of the dot scales with the intensity of the plastic deformation events.

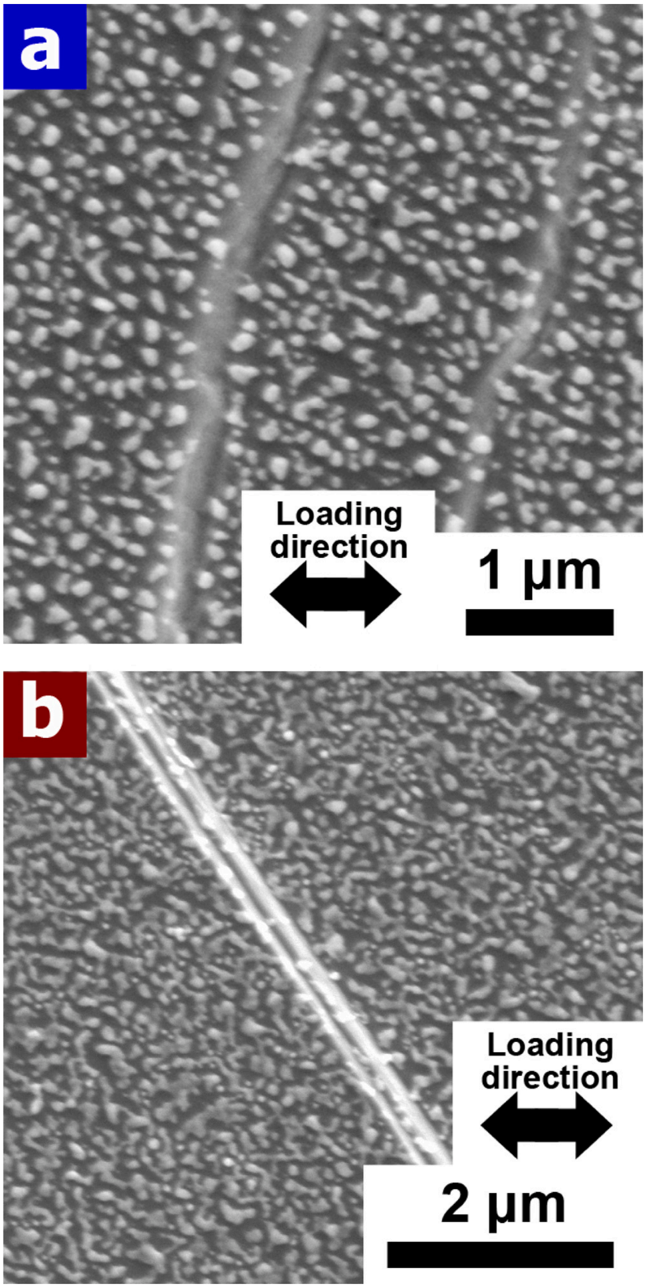

Fig. 17. High-resolution SEM images at the surface of a specimen after deformation at liquid helium temperature showing wavy slip **(a)**. Infrequent closely-spaced slip was observed after room temperature deformation **(b)**. The visible nanoscale particles are the speckle pattern employed for HR-DIC.

become substantial at the grain boundary, potentially generalizing the rare behavior (closely-spaced slip) observed after deformation at room temperature.

At liquid helium temperatures, a less commonly studied deformation process associated with the discontinuous plastic flow, i.e., serrated yielding, also referred to as low-temperature serrated deformation, is typically mentioned in FCC materials near absolute zero [61–65]. The significant stress drops observed in the plastic regime of the curve for the liquid helium test, as observed in Fig. 1(d), provide clear evidence of this phenomenon. This phenomenon is thought to arise from either a transition from screw to edge dislocation glide and catastrophic failure of lattice barriers [56,61], or from local adiabatic heating [89]. However, DPF is not observed under deformation at liquid nitrogen temperature, and the associated avalanche multiplication was never experimentally studied at liquid helium temperatures. Consequently, it is unclear whether the fundamental deformation mechanisms involved in the observed slip delocalization differ between liquid nitrogen and helium temperatures, and if the discontinuous plastic flow contributes to increased slip delocalization. The observed increase in slip delocalization at liquid helium temperatures, indicated by thicker deformation events (see Fig. 8) and a high contribution of <112> shearing, might be simply attributed to a decrease in stacking fault energy from liquid nitrogen to liquid helium temperatures facilitating deformation twinning. Further research is needed to clarify this aspect.

Interestingly, the occurrence of slip delocalization at cryogenic temperature may explain the improved fatigue properties usually observed for FCC materials tested at cryogenic temperatures [6]. Usually, the fatigue ratio at cryogenic temperatures is higher than that at room temperature [6]. It should be a surprise since the increase in yield strength at cryogenic temperatures should result in significantly higher surface slip step, usually facilitating fatigue crack nucleation and reducing fatigue strength [42]. The identified slip delocalization mechanisms prevent the formation of large surface slip steps and locally homogenize the deformation that may delay fatigue crack initiation.

4.3. Temperature dependence of microstructural effects

The microstructural features responsible for the most intense deformation events are consistently found in a parallel slip configuration across all investigated temperatures. This configuration is inducing incipient and intense plastic deformation localization at room temperature in nickel-based superalloys [82], including 718 superalloys [60]. Factors such as extended length of annealing twin boundaries, elastic anisotropy, or high resolved shear stress promote dislocation glide along planes close to and parallel to coherent twin boundaries at room temperature [90]. Interestingly, this behavior is also observed at liquid nitrogen and helium temperatures, as shown in Fig. 16. Intense plastic deformation localization occurs both near and parallel to twin boundaries, characterized by two scenarios: one where there is intense directional misorientation across the twin boundary, associated with a low Schmid factor for <110> slip directions and a high mismatch in directional elastic modulus; and another where there is low directional misorientation at the twin boundary, associated with a high Schmid factor for a <110> slip direction and a small mismatch in directional elastic modulus. The distributions of directional misorientation across twin boundaries in Fig. 16(c), which induced the most intense events, cover all possible misorientations for all investigated temperatures. This confirms the similar effects of Schmid factor and elastic modulus at cryogenic temperatures as reported at room temperature [82,90]. Such behavior can be explained considering that dislocation slip is the dominant mode at low levels of deformation, as demonstrated in this study, and that the elastic anisotropy at cryogenic temperatures may be significant as observed at room temperature for the 718 superalloys [91].

5. Conclusions

Plastic deformation localization and microstructural effects were investigated using high-resolution digital image correlation and high-resolution scanning transmission electron microscopy during monotonic deformation at room, liquid nitrogen, and liquid helium temperatures on an FCC polycrystalline Ni-based superalloy material. We highlight distinct deformation mechanisms that control plastic deformation localization at cryogenic temperatures. The following conclusions are drawn.

- Under deformation at cryogenic temperatures, competing deformation mechanisms such as slip, deformation twinning, stacking faults, and hexagonal-close packed regions occur in the nickel-based superalloy 718.

- While deformation twinning is prevalent at high levels of deformation, slip is the dominant mechanism at lower deformation levels at both liquid nitrogen and liquid helium temperatures.
- Deformation events at room temperature typically feature a single slip band, whereas closely-spaced slip bands are common at cryogenic temperatures. This leads to a phenomenon of plastic deformation delocalization at these lower temperatures, resulting in a local homogenization of plasticity through the formation of closely-spaced slip bands of relatively low intensities.
- The microstructural configurations that promote intense plastic deformation localization at low levels of deformation are observed to be similar across the room and cryogenic temperatures and associated with annealing twins.

CRediT authorship contribution statement

Dhruv Anjaria: Writing – original draft, Writing – review & editing, Validation, Methodology, Investigation, Formal analysis, Data curation, Conceptualization. **Milan Heczko:** Writing – review & editing, Investigation. **Rephayah L. Black:** Investigation. **Chris Bean:** Writing – original draft, Writing – review & editing. **Mike A. Reynolds:** Writing – review & editing. **Kun Zhang:** Writing – review & editing. **Damien Texier:** Writing – review & editing. **Valery Valle:** Software. **Michael J. Mills:** Writing – review & editing. **Darren C. Pagan:** Writing – review & editing. **J.C. Stinville:** Writing – original draft, Writing – review & editing, Visualization, Validation, Supervision, Project administration, Methodology, Investigation, Funding acquisition, Formal analysis, Data curation, Conceptualization.

Declaration of competing interest

The authors declare that they have no known competing financial interests or personal relationships that could have appeared to influence the work reported in this paper.

Data availability

The data that support the findings of the present study are available in the data repository Dryad [57].

Acknowledgments

DA and JCS acknowledge the support of the National Science Foundation (NSF), USA: DMR Grant #2234892. CB, RLB, and JCS are grateful for financial support from the Energy & Biosciences Institute (EBI), USA, through the EBI-Shell Program. DCP is supported by NSF Award DMR, USA Grant #2234891. This work was carried out in the Materials Research Laboratory Central Research Facilities, University of Illinois, and at the Advanced Materials Testing and Evaluation Laboratory, University of Illinois. Scanning transmission electron microscopy was performed at the Center for Electron Microscopy and Analysis (CEMAS) at The Ohio State University. Special thanks to Eric Thorsland for his technical assistance. Carpenter Technology are acknowledged for providing the 718 material. DT and JCS are grateful to the Centre National de la Recherche Scientifique (CNRS), France for the mobility grant with the International Research Project denoted "CIN&MAT". The color-blind version of this article has been made possible thanks to funding from the National Science Foundation (NSF), USA (award #2338346).

Appendix A. Supplementary data

Supplementary material related to this article can be found online at https://doi.org/10.1016/j.actamat.2024.120106.

References

[1] Johannes Schindelin, Ignacio Arganda-Carreras, Erwin Frise, Verena Kaynig, Mark Longair, Tobias Pietzsch, Stephan Preibisch, Curtis Rueden, Stephan Saalfeld, Benjamin Schmid, Jean-Yves Tinevez, Daniel James White, Volker Hartenstein, Kevin Eliceiri, Pavel Tomancak, Albert Cardona, Fiji: an open-source platform for biological-image analysis, Nat. Methods (ISSN: 1548-7105) 9 (7) (2012) 676–682, http://dx.doi.org/10.1038/nmeth.2019.

[2] Joachim Goedhart, Material related to the blog that reports on the parrot LUT, Zenodo (2018) http://dx.doi.org/10.5281/zenodo.1211690.

[3] H. Barthelemy, M. Weber, F. Barbier, Hydrogen storage: Recent improvements and industrial perspectives, Int. J. Hydrog. Energy (ISSN: 0360-3199) 42 (11) (2017) 7254–7262, http://dx.doi.org/10.1016/j.ijhydene.2016.03.178, URL https://www.sciencedirect.com/science/article/pii/S0360319916305559, Special issue on The 6th International Conference on Hydrogen Safety (ICHS 2015), 19-21 October 2015, Yokohama, Japan.

[4] E. David, Materials for cryogenics applications, in: Proceedings of the 12th International Scientific Conference Achievements in Mechanical & Materials Engineering, Polish Academy of Sciences - Committee of Materials Science, Silesian University of Technology of Gliwice, Institute of Engineering Materials and Biomaterials, Association of Alumni of Silesian University of Technology, 2003, Research National Institute for Cryogenics & Isotopic Technologies, Rm. Valcea, P.O. Box 10, O.P. No. 4, Code 1000, Romania.

[5] C. Spenny, D. Van Matre, J. Haislip, R. Linscott, W. Raynes, M. Skinner, An aluminum salvage station for external tanks of the space shuttle, Acta Astronaut. (ISSN: 0094-5765) 29 (5) (1993) 379–397, http://dx.doi.org/10.1016/0094-5765(93)90022-O, URL https://www.sciencedirect.com/science/article/pii/009457659390022O.

[6] Yoshinori Ono, Tetsumi Yuri, Hideshi Sumiyoshi, Etsuo Takeuchi, Saburo Matsuoka, Toshio Ogata, High-cycle fatigue properties at cryogenic temperatures in INCONEL 718 nickel-based superalloy, 2004, URL https://api.semanticscholar.org/CorpusID:54683638.

[7] Nitesh Raj Jaladurgam, Saurabh Kabra, Magnus Hörnqvist Colliander, Macro- and micro-mechanical behaviour of a strengthened Ni-based superalloy at cryogenic temperatures, Mater. Des. (ISSN: 0264-1275) 209 (2021) 109954, http://dx.doi.org/10.1016/j.matdes.2021.109954, URL https://www.sciencedirect.com/science/article/pii/S0264127521005086.

[8] Q. Ding, H. Bei, X. Wei, Y.F. Gao, Z. Zhang, Nano-twin-induced exceptionally superior cryogenic mechanical properties of a Ni-based GH3536 (Hastelloy X) superalloy, Mater. Today Nano (ISSN: 2588-8420) 14 (2021) 100110, http://dx.doi.org/10.1016/j.mtnano.2021.100110, URL https://www.sciencedirect.com/science/article/pii/S258884202100002X.

[9] Joakim Nordström, Raveendra Siriki, Mattias Calmunger, Johan Moverare, Guocai Chai, TWIP and fracture behavior in the superalloy 625 at room and cryogenic temperatures, Proc. Struct. Integr. (ISSN: 2452-3216) 23 (2019) 457–462, http://dx.doi.org/10.1016/j.prostr.2020.01.129, URL https://www.sciencedirect.com/science/article/pii/S2452321620301955, 9th International Conference Materials Structure & Micromechanics of Fracture (MSMF9).

[10] Shuyong Jiang, Dong Sun, Yanqiu Zhang, Xiaoming Zhu, Man Wang, Chengzhi Zhao, Plastic deformation mechanisms of NiCuCrMoTiAlNb Ni-based alloys at cryogenic temperature, Mater. Sci. Eng. A (ISSN: 0921-5093) 664 (2016) 135–145, http://dx.doi.org/10.1016/j.msea.2016.03.133, URL https://www.sciencedirect.com/science/article/pii/S0921509316303604.

[11] Bernd Gludovatz, Anton Hohenwarter, Keli V.S. Thurston, Hongbin Bei, Zhenggang Wu, Easo P. George, Robert O. Ritchie, Exceptional damage-tolerance of a medium-entropy alloy CrCoNi at cryogenic temperatures, Nature Commun. (ISSN: 2041-1723) 7 (1) (2016) 10602, http://dx.doi.org/10.1038/ncomms10602.

[12] Z.W. Huang, S.B. Jin, H. Zhou, Y.S. Li, Y. Cao, Y.T. Zhu, Evolution of twinning systems and variants during sequential twinning in cryo-rolled titanium, Int. J. Plast. (ISSN: 0749-6419) 112 (2019) 52–67, http://dx.doi.org/10.1016/j.ijplas.2018.08.008, URL https://www.sciencedirect.com/science/article/pii/S0749641918300809.

[13] J.W. Christian, S. Mahajan, Deformation twinning, Prog. Mater. Sci. (ISSN: 0079-6425) 39 (1) (1995) 1–157, http://dx.doi.org/10.1016/0079-6425(94)00007-7, URL https://www.sciencedirect.com/science/article/pii/0079642594000077.

[14] Tian Ye, Feng Zhao, Lianyang Chen, Kun Jiang, Qiong Deng, Yuzeng Chen, Qingyuan Wang, Tao Suo, Effect of strain rate and low temperature on mechanical behaviour and microstructure evolution in twinning-induced plasticity steel, Mater. Sci. Eng. A (ISSN: 0921-5093) 823 (2021) 141734, http://dx.doi.org/10.1016/j.msea.2021.141734, URL https://www.sciencedirect.com/science/article/pii/S0921509321010029.

[15] Le Li, Zhenghao Chen, Shogo Kuroiwa, Mitsuhiro Ito, Kyosuke Kishida, Haruyuki Inui, Easo P. George, Tensile and compressive plastic deformation behavior of medium-entropy Cr-Co-Ni single crystals from cryogenic to elevated temperatures, Int. J. Plast. (ISSN: 0749-6419) 148 (2022) 103144, http://dx.doi.org/10.1016/j.ijplas.2021.103144, URL https://www.sciencedirect.com/science/article/pii/S0749641921002126.

[16] Y.X. Li, Raymond Kwesi Nutor, Q.K. Zhao, X.P. Zhang, Q.P. Cao, S.S. Sohn, X.D. Wang, S.Q. Ding, D.X. Zhang, H.F. Zhou, J.W. Wang, J.Z. Jiang, Unraveling the deformation behavior of the Fe45Co25Ni10V20 high entropy alloy, Int. J. Plast. (ISSN: 0749-6419) 165 (2023) 103619, http://dx.doi.org/10.1016/j.ijplas.2023.103619, URL https://www.sciencedirect.com/science/article/pii/S0749641923001055.

[17] Qingqing Ding, Xiaoqian Fu, Dengke Chen, Hongbin Bei, Bernd Gludovatz, Jixue Li, Ze Zhang, Easo P. George, Qian Yu, Ting Zhu, Robert O. Ritchie, Real-time nanoscale observation of deformation mechanisms in CrCoNi-based medium-to high-entropy alloys at cryogenic temperatures, Mater. Today (ISSN: 1369-7021) 25 (2019) 21–27, http://dx.doi.org/10.1016/j.mattod.2019.03.001, URL https://www.sciencedirect.com/science/article/pii/S1369702118313592.

[18] Milan Heczko, Veronika Mazánová, Connor E. Slone, Mulaine Shih, Easo P. George, Maryam Ghazisaeidi, Jaroslav Polák, Michael J. Mills, Role of deformation twinning in fatigue of CrCoNi medium-entropy alloy at room temperature, Scr. Mater. 202 (2021) 113985.

[19] Ritesh Jagatramka, Matthew Daly, The competition between deformation twinning and dislocation slip in deformed face-centered cubic metals, JOM (ISSN: 1543-1851) 74 (10) (2022) 3799–3810, http://dx.doi.org/10.1007/s11837-022-05437-3.

[20] O. Grässel, L. Krüger, G. Frommeyer, L.W. Meyer, High strength Fe–Mn–(Al, Si) TRIP/TWIP steels development — properties — application, Int. J. Plast. (ISSN: 0749-6419) 16 (10) (2000) 1391–1409, http://dx.doi.org/10.1016/S0749-6419(00)00015-2, URL https://www.sciencedirect.com/science/article/pii/S0749641900000152.

[21] I. Gutierrez-Urrutia, S. Zaefferer, D. Raabe, The effect of grain size and grain orientation on deformation twinning in a Fe–22wt.% Mn–0.6wt.% C TWIP steel, Mater. Sci. Eng. A (ISSN: 0921-5093) 527 (15) (2010) 3552–3560, http://dx.doi.org/10.1016/j.msea.2010.02.041, URL https://www.sciencedirect.com/science/article/pii/S0921509310001917.

[22] K. Lu, L. Lu, S. Suresh, Strengthening materials by engineering coherent internal boundaries at the nanoscale, Science 324 (5925) (2009) 349–352, http://dx.doi.org/10.1126/science.1159610, arXiv:https://www.science.org/doi/pdf/10.1126/science.1159610, URL https://www.science.org/doi/abs/10.1126/science.1159610.

[23] Y. Deng, C.C. Tasan, K.G. Pradeep, H. Springer, A. Kostka, D. Raabe, Design of a twinning-induced plasticity high entropy alloy, Acta Mater. (ISSN: 1359-6454) 94 (2015) 124–133, http://dx.doi.org/10.1016/j.actamat.2015.04.014, URL https://www.sciencedirect.com/science/article/pii/S1359645415002566.

[24] M. Bönisch, Y. Wu, H. Sehitoglu, Hardening by slip-twin and twin-twin interactions in FeMnNiCoCr, Acta Mater. (ISSN: 1359-6454) 153 (2018) 391–403, http://dx.doi.org/10.1016/j.actamat.2018.04.054, URL https://www.sciencedirect.com/science/article/pii/S1359645418303318.

[25] Fabio Di Gioacchino, João Quinta da Fonseca, An experimental study of the polycrystalline plasticity of austenitic stainless steel, Int. J. Plast. (ISSN: 0749-6419) 74 (2015) 92–109, http://dx.doi.org/10.1016/j.ijplas.2015.05.012, URL http://www.sciencedirect.com/science/article/pii/S0749641915000820.

[26] J.C. Stinville, M.P. Echlin, D. Texier, F. Bridier, P. Bocher, T.M. Pollock, Sub-grain scale digital image correlation by electron microscopy for polycrystalline materials during elastic and plastic deformation, Exp. Mech. (ISSN: 0014-4851) (2015) 1–20, http://dx.doi.org/10.1007/s11340-015-0083-4.

[27] J.C. Stinville, W. Ludwig, P.G. Callahan, M.P. Echlin, V. Valle, T.M. Pollock, H. Proudhon, Observation of bulk plasticity in a polycrystalline titanium alloy by diffraction contrast tomography and topotomography, Mater. Charact. (ISSN: 1044-5803) 188 (2022) 111891, http://dx.doi.org/10.1016/j.matchar.2022.111891, URL https://www.sciencedirect.com/science/article/pii/S1044580322001735.

[28] Darren C. Pagan, Kelly E. Nygren, Matthew P. Miller, Analysis of a three-dimensional slip field in a hexagonal Ti alloy from in-situ high-energy X-ray diffraction microscopy data, Acta Mater. (ISSN: 1359-6454) 221 (2021) 117372, http://dx.doi.org/10.1016/j.actamat.2021.117372, URL https://www.sciencedirect.com/science/article/pii/S1359645421007515.

[29] Christopher M. Magazzeni, Hazel M. Gardner, Inigo Howe, Phillip Gopon, John C. Waite, David Rugg, David E.J. Armstrong, Angus J. Wilkinson, Nanoindentation in multi-modal map combinations: a correlative approach to local mechanical property assessment, J. Mater. Res. (ISSN: 2044-5326) 36 (11) (2021) 2235–2250, http://dx.doi.org/10.1557/s43578-020-00035-y.

[30] S. Moore, R. Burrows, D. Kumar, M.B. Kloucek, A.D. Warren, P.E.J. Flewitt, L. Picco, O.D. Payton, T.L. Martin, Observation of stress corrosion cracking using real-time in situ high-speed atomic force microscopy and correlative techniques, npj Mater. Degrad. 5 (1) (2021) http://dx.doi.org/10.1038/s41529-020-00149-y.

[31] Henry Proudhon, Nicolas Guéninchault, Samuel Forest, Wolfgang Ludwig, Incipient bulk polycrystal plasticity observed by synchrotron in-situ topotomography, Materials (ISSN: 1996-1944) 11 (10) (2018) http://dx.doi.org/10.3390/ma11102018, URL https://www.mdpi.com/1996-1944/11/10/2018.

[32] Daniel S. Gianola, T. Ben Britton, Stefan Zaefferer, New techniques for imaging and identifying defects in electron microscopy, MRS Bull. 44 (06) (2019) 450–458, http://dx.doi.org/10.1557/mrs.2019.125.

[33] T.B. Britton, A.J. Wilkinson, Measurement of residual elastic strain and lattice rotations with high resolution electron backscatter diffraction, Ultramicroscopy (ISSN: 0304-3991) 111 (8) (2011) 1395–1404, http://dx.doi.org/10.1016/j.ultramic.2011.05.007, URL https://www.sciencedirect.com/science/article/pii/S0304399111001665.

[34] Zhen Zhang, David Lunt, Hamidreza Abdolvand, Angus J. Wilkinson, Michael Preuss, Fionn P.E. Dunne, Quantitative investigation of micro slip and localization in polycrystalline materials under uniaxial tension, Int. J. Plast. (ISSN: 0749-6419) 108 (2018) 88–106, http://dx.doi.org/10.1016/j.ijplas.2018.04.014, URL https://www.sciencedirect.com/science/article/pii/S0749641917307064.

[35] Marissa A. Linne, Thomas R. Bieler, Samantha Daly, The effect of microstructure on the relationship between grain boundary sliding and slip transmission in high purity aluminum, Int. J. Plast. (ISSN: 0749-6419) 135 (2020) 102818, http://dx.doi.org/10.1016/j.ijplas.2020.102818, URL https://www.sciencedirect.com/science/article/pii/S0749641920300152.

[36] Y. Wu, M. Bönisch, S. Alkan, W. Abuzaid, H. Sehitoglu, Experimental determination of latent hardening coefficients in FeMnNiCoCr, Int. J. Plast. (ISSN: 0749-6419) 105 (2018) 239–260, http://dx.doi.org/10.1016/j.ijplas.2018.02.016, URL https://www.sciencedirect.com/science/article/pii/S074964191730668X.

[37] C. Efstathiou, H. Sehitoglu, J. Lambros, Multiscale strain measurements of plastically deforming polycrystalline titanium: Role of deformation heterogeneities, Int. J. Plast. (ISSN: 0749-6419) 26 (1) (2010) 93–106, http://dx.doi.org/10.1016/j.ijplas.2009.04.006, URL https://www.sciencedirect.com/science/article/pii/S0749641909000771.

[38] F. Bourdin, J.C. Stinville, M.P. Echlin, P.G. Callahan, W.C. Lenthe, C.J. Torbet, D. Texier, F. Bridier, J. Cormier, P. Villechaise, T.M. Pollock, V. Valle, Measurements of plastic localization by heaviside-digital image correlation, Acta Mater. (ISSN: 1359-6454) 157 (2018) 307–325, http://dx.doi.org/10.1016/j.actamat.2018.07.013, URL http://www.sciencedirect.com/science/article/pii/S135964541830541X.

[39] Z. Chen, S.H. Daly, Active slip system identification in polycrystalline metals by digital image correlation (DIC), Exp. Mech. (ISSN: 1741-2765) 57 (1) (2017) 115–127, http://dx.doi.org/10.1007/s11340-016-0217-3.

[40] Allan Harte, Michael Atkinson, Albert Smith, Carsten Drouven, Stefan Zaefferer, João Quinta da Fonseca, Michael Preuss, The effect of solid solution and gamma prime on the deformation modes in Ni-based superalloys, Acta Mater. (ISSN: 1359-6454) 194 (2020) 257–275, http://dx.doi.org/10.1016/j.actamat.2020.04.004, URL https://www.sciencedirect.com/science/article/pii/S1359645420302615.

[41] Z. Chen, S. Daly, Deformation twin identification in magnesium through clustering and computer vision, Mater. Sci. Eng. A (ISSN: 0921-5093) 736 (2018) 61–75, http://dx.doi.org/10.1016/j.msea.2018.08.083, URL https://www.sciencedirect.com/science/article/pii/S0921509318311584.

[42] J.C. Stinville, M.A. Charpagne, A. Cervellon, S. Hemery, F. Wang, P.G. Callahan, V. Valle, T.M. Pollock, On the origins of fatigue strength in crystalline metallic materials, Science 377 (6610) (2022) 1065–1071, http://dx.doi.org/10.1126/science.abn0392, arXiv:https://www.science.org/doi/pdf/10.1126/science.abn0392, URL https://www.science.org/doi/abs/10.1126/science.abn0392.

[43] Zhenbo Zhang, Zhibiao Yang, Song Lu, Allan Harte, Roberto Morana, Michael Preuss, Strain localisation and failure at twin-boundary complexions in nickel-based superalloys, Nature Commun. (ISSN: 2041-1723) 11 (1) (2020) 4890, http://dx.doi.org/10.1038/s41467-020-18641-z.

[44] Anja Weidner, Horst Biermann, Review on strain localization phenomena studied by high-resolution digital image correlation, Adv. Eng. Mater. 23 (4) (2021) 2001409, http://dx.doi.org/10.1002/adem.202001409, arXiv:https://onlinelibrary.wiley.com/doi/pdf/10.1002/adem.202001409, URL https://onlinelibrary.wiley.com/doi/abs/10.1002/adem.202001409.

[45] T. Vermeij, C.J.A. Mornout, V. Rezazadeh, J.P.M. Hoefnagels, Martensite plasticity and damage competition in dual-phase steel: A micromechanical experimental-numerical study, Acta Mater. (ISSN: 1359-6454) (2023) 119020, http://dx.doi.org/10.1016/j.actamat.2023.119020, URL https://www.sciencedirect.com/science/article/pii/S1359645423003518.

[46] P.-A. Juan, S. Berbenni, M.R. Barnett, C.N. Tomé, L. Capolungo, A double inclusion homogenization scheme for polycrystals with hierarchal topologies: application to twinning in Mg alloys, Int. J. Plast. (ISSN: 0749-6419) 60 (2014) 182–196, http://dx.doi.org/10.1016/j.ijplas.2014.04.001, URL https://www.sciencedirect.com/science/article/pii/S0749641914000722.

[47] J.D. Carroll, L.N. Brewer, C.C. Battaile, B.L. Boyce, J.M. Emery, The effect of grain size on local deformation near a void-like stress concentration, Int. J. Plast. (ISSN: 0749-6419) 39 (2012) 46–60, http://dx.doi.org/10.1016/j.ijplas.2012.06.002, URL https://www.sciencedirect.com/science/article/pii/S0749641912000964.

[48] Thomas Edward James Edwards, Fabio Di Gioacchino, William John Clegg, An experimental study of the polycrystalline plasticity of lamellar titanium aluminide, Int. J. Plast. (ISSN: 0749-6419) 118 (2019) 291–319, http://dx.doi.org/10.1016/j.ijplas.2019.02.013, URL https://www.sciencedirect.com/science/article/pii/S0749641918304984.

[49] D.C. Stouffer, L.T. Dame, Inelastic Deformation of Metals: Models, Mechanical Properties, and Metallurgy, Wiley, ISBN: 9780471021438, 1996, URL https://books.google.com/books?id=P2ON6ykaW7UC.

[50] Shailesh Patel, John deBarbadillo, Stephen Coryell, Superalloy 718: Evolution of the alloy from high to low temperature application, in: Eric Ott, Xingbo Liu, Joel Andersson, Zhongnan Bi, Kevin Bockenstedt, Ian Dempster, Jon Groh, Karl Heck, Paul Jablonski, Max Kaplan, Daisuke Nagahama, Chantal Sudbrack (Eds.), Proceedings of the 9th International Symposium on Superalloy 718 & Derivatives: Energy, Aerospace, and Industrial Applications, Springer International Publishing, Cham, ISBN: 978-3-319-89480-5, 2018, pp. 23–49.

[51] Roger C. Reed, The Superalloys: Fundamentals and Applications, Cambridge University Press, ISBN: 9780511541285, 2006, http://dx.doi.org/10.1017/cbo9780511541285.

[52] M. Sundararaman, P. Mukhopadhyay, S. Banerjee, Deformation behaviour of γ'' strengthened inconel 718, Acta Metall. (ISSN: 0001-6160) 36 (4) (1988) 847–864, http://dx.doi.org/10.1016/0001-6160(88)90139-3, URL https://www.sciencedirect.com/science/article/pii/0001616088901393.

[53] Prafull Pandey, Milan Heczko, Nikhil Khatavkar, Namrata Mazumder, Abhishek Sharma, Abhishek Singh, Michael J. Mills, Kamanio Chattopadhyay, On the faulting and twinning mediated strengthening and plasticity in a strengthened CoNi-based superalloy at room temperature, Acta Mater. (ISSN: 1359-6454) 252 (2023) 118928, http://dx.doi.org/10.1016/j.actamat.2023.118928, URL https://www.sciencedirect.com/science/article/pii/S1359645423002598.

[54] A.H. Cottrell, The Nabarro equation for thermally activated plastic glide, Phil. Mag. 86 (25–26) (2006) 3811–3817, http://dx.doi.org/10.1080/14786430500380118.

[55] K. Srivastava, D. Weygand, D. Caillard, P. Gumbsch, Repulsion leads to coupled dislocation motion and extended work hardening in bcc metals, Nature Commun. 11 (1) (2020) 5098.

[56] J. Tabin, B. Skoczen, J. Bielski, Strain localization during discontinuous plastic flow at extremely low temperatures, Int. J. Solids Struct. (ISSN: 0020-7683) 97–98 (2016) 593–612, http://dx.doi.org/10.1016/j.ijsolstr.2016.06.012, URL https://www.sciencedirect.com/science/article/pii/S0020768316301275.

[57] Dhruv Anjaria, Rephayah Black, Chris Bean, Jean-Charles Stinville, High resolution dataset of plastic deformation at cryogenic temperatures in a nickel-based superalloy, 2024, http://dx.doi.org/10.5061/DRYAD.JM63XSJK3, https://datadryad.org/stash/dataset/doi:10.5061/dryad.jm63xsjk3.

[58] J.H. Liu, N. Vanderesse, J.-C. Stinville, T.M. Pollock, P. Bocher, D. Texier, In-plane and out-of-plane deformation at the sub-grain scale in polycrystalline materials assessed by confocal microscopy, Acta Mater. 169 (2019) 260–274, http://dx.doi.org/10.1016/j.actamat.2019.03.001.

[59] J.C. Stinville, J.M. Hestroffer, M.A. Charpagne, A.T. Polonsky, M.P. Echlin, C.J. Torbet, V. Valle, K.E. Nygren, M.P. Miller, O. Klaas, A. Loghin, I.J. Beyerlein, T.M. Pollock, Multi-modal dataset of a polycrystalline metallic material: 3D microstructure and deformation fields, Sci. Data (ISSN: 2052-4463) 9 (1) (2022) 460, http://dx.doi.org/10.1038/s41597-022-01525-w.

[60] M.A. Charpagne, J.M. Hestroffer, A.T. Polonsky, M.P. Echlin, D. Texier, V. Valle, I.J. Beyerlein, T.M. Pollock, J.C. Stinville, Slip localization in Inconel 718: A three-dimensional and statistical perspective, Acta Mater. (ISSN: 1359-6454) 215 (2021) 117037, http://dx.doi.org/10.1016/j.actamat.2021.117037, URL https://www.sciencedirect.com/science/article/pii/S1359645421004171.

[61] B. Obst, A. Nyilas, Experimental evidence on the dislocation mechanism of serrated yielding in f.c.c. metals and alloys at low temperatures, Mater. Sci. Eng. A (ISSN: 0921-5093) 137 (1991) 141–150, http://dx.doi.org/10.1016/0921-5093(91)90328-K, URL https://www.sciencedirect.com/science/article/pii/092150939190328K, Fifth International Symposium on Plasticity of Metals and Alloys.

[62] Niraj Nayan, S.V.S. Narayana Murty, A.K. Jha, Bhanu Pant, S.C. Sharma, K.M. George, G.V.S. Sastry, Mechanical properties of aluminium-copper-lithium alloy AA2195 at cryogenic temperatures, Mater. Des. 58 (2014) 445–450, http://dx.doi.org/10.1016/j.matdes.2014.02.024.

[63] E.M. Medvedev, On the character of low temperature discontinuous plastic deformation of metals, Cryogenics 16 (9) (1976) 533–536, http://dx.doi.org/10.1016/0011-2275(76)90300-3.

[64] Z.S. Basinski, The instability of plastic flow of metals at very low temperatures. II., Aust. J. Phys. 13 (2) (1960) 354, http://dx.doi.org/10.1071/ph600354a.

[65] Yu. Ivanisenko, E.D. Tabachnikova, I.A. Psaruk, S.N. Smirnov, A. Kilmametov, A. Kobler, C. Kübel, L. Kurmanaeva, K. Csach, Y. Mishkuf, T. Scherer, Y.A. Semerenko, H. Hahn, Variation of the deformation mechanisms in a nanocrystalline pd–10at, Int. J. Plast. (ISSN: 0749-6419) 60 (2014) 40–57, http://dx.doi.org/10.1016/j.ijplas.2014.04.011, URL https://www.sciencedirect.com/science/article/pii/S0749641914000941.

[66] M.A. Charpagne, J.C. Stinville, P.G. Callahan, D. Texier, Z. Chen, P. Villechaise, V. Valle, T.M. Pollock, Automated and quantitative analysis of plastic strain localization via multi-modal data recombination, Mater. Charact. (ISSN: 1044-5803) 163 (2020) 110245, http://dx.doi.org/10.1016/j.matchar.2020.110245, URL https://www.sciencedirect.com/science/article/pii/S1044580319335569.

[67] P.J. Phillips, M.C. Brandes, M.J. Mills, M. De Graef, Diffraction contrast STEM of dislocations: Imaging and simulations, Ultramicroscopy (ISSN: 0304-3991) 111 (9) (2011) 1483–1487, http://dx.doi.org/10.1016/j.ultramic.2011.07.001, URL https://www.sciencedirect.com/science/article/pii/S0304399111001781.

[68] Changning Niu, Carlyn R. LaRosa, Jiashi Miao, Michael J. Mills, Maryam Ghazisaeidi, Magnetically-driven phase transformation strengthening in high entropy alloys, Nature Commun. (ISSN: 2041-1723) 9 (1) (2018) 1363, http://dx.doi.org/10.1038/s41467-018-03846-0.

[69] C.B. Montgomery, B. Koohbor, N.R. Sottos, A robust patterning technique for electron microscopy-based digital image correlation at sub-micron resolutions, Exp. Mech. 59 (7) (2019) 1063–1073, http://dx.doi.org/10.1007/s11340-019-00487-2.

[70] A.D. Kammers, S. Daly, Digital image correlation under scanning electron microscopy: Methodology and validation, Exp. Mech. (ISSN: 0014-4851) 53 (9) (2013) 1743–1761, http://dx.doi.org/10.1007/s11340-013-9782-x, URL http://dx.doi.org/10.1007/s11340-013-9782-x.

[71] J.C. Stinville, T. Francis, A.T. Polonsky, C.J. Torbet, M.A. Charpagne, Z. Chen, G.H. Balbus, F. Bourdin, V. Valle, P.G. Callahan, M.P. Echlin, T.M. Pollock, Time-resolved digital image correlation in the scanning electron microscope for analysis of time-dependent mechanisms, Exp. Mech. (ISSN: 1741-2765) 61 (2) (2021) 331–348, http://dx.doi.org/10.1007/s11340-020-00632-2.

[72] Jean Charles Stinville, Etienne Martin, Mallikarjun Karadge, Shak Ismonov, Monica Soare, Tim Hanlon, Sairam Sundaram, McLean P. Echlin, Patrick G. Callahan, William C. Lenthe, V.M. Miller, Jiashi Miao, Andrew E. Wessman, Rebecca Finlay, Adrian Loghin, Judson Marte, Tresa M. Pollock, Fatigue deformation in a polycrystalline nickel base superalloy at intermediate and high temperature: Competing failure modes, Acta Mater. (ISSN: 1359-6454) 152 (2018) 16–33, http://dx.doi.org/10.1016/j.actamat.2018.03.035, URL http://www.sciencedirect.com/science/article/pii/S1359645418302337.

[73] A. Harte, M. Atkinson, M. Preuss, J. Quinta da Fonseca, A statistical study of the relationship between plastic strain and lattice misorientation on the surface of a deformed Ni-based superalloy, Acta Mater. (ISSN: 1359-6454) 195 (2020) 555–570, http://dx.doi.org/10.1016/j.actamat.2020.05.029, URL https://www.sciencedirect.com/science/article/pii/S1359645420303761.

[74] George Ellwood Dieter, David Bacon, Mechanical Metallurgy, vol. 3, McGraw-hill New York, 1976.

[75] Valéry Valle, Stephen Hedan, Philippe Cosenza, Anne-Laure Fauchille, M. Berdjane, DIC development for the study of materials including multiple crossing cracks, Exp. Mech. (ISSN: 17412765) 55 (2) (2015) 379–391, http://dx.doi.org/10.1007/s11340-014-9948-1.

[76] Alexander Bergsmo, Yilun Xu, Benjamin Poole, Fionn P.E. Dunne, Twin boundary fatigue crack nucleation in a polycrystalline nickel superalloy containing non-metallic inclusions, J. Mech. Phys. Solids (ISSN: 0022-5096) 160 (2022) 104785, http://dx.doi.org/10.1016/j.jmps.2022.104785, URL https://www.sciencedirect.com/science/article/pii/S0022509622000084.

[77] C. Bean, F. Wang, M.A. Charpagne, P. Villechaise, V. Valle, S.R. Agnew, D.S. Gianola, T.M. Pollock, J.C. Stinville, Heterogeneous slip localization in an additively manufactured 316l stainless steel, Int. J. Plast. (ISSN: 0749-6419) 159 (2022) 103436, http://dx.doi.org/10.1016/j.ijplas.2022.103436, URL https://www.sciencedirect.com/science/article/pii/S0749641922002145.

[78] Hael Mughrabi, Cyclic slip irreversibilities and the evolution of fatigue damage, Metall. Mater. Trans. A (ISSN: 1543-1940) 40 (6) (2009) 1257–1279, http://dx.doi.org/10.1007/s11661-009-9839-8, URL http://dx.doi.org/10.1007/s11661-009-9839-8.

[79] J.C. Stinville, P.G. Callahan, M.A. Charpagne, M.P. Echlin, V. Valle, T.M. Pollock, Direct measurements of slip irreversibility in a nickel-based superalloy using high resolution digital image correlation, Acta Mater. (ISSN: 1359-6454) 186 (2020) 172–189, http://dx.doi.org/10.1016/j.actamat.2019.12.009, URL http://www.sciencedirect.com/science/article/pii/S1359645419308389.

[80] R.L. Black, D. Anjaria, J. Genée, V. Valle, J.C. Stinville, Micro-strain and cyclic slip accumulation in a polycrystalline nickel-based superalloy, Acta Mater. (ISSN: 1359-6454) 266 (2024) 119657, http://dx.doi.org/10.1016/j.actamat.2024.119657, URL https://www.sciencedirect.com/science/article/pii/S1359645424000107.

[81] Longsheng Feng, Rongpei Shi, Christopher H. Zenk, Michael J. Mills, Yunzhi Wang, Phase field modeling of shearing processes of a dual-lobed coprecipitate, Acta Mater. (ISSN: 1359-6454) 246 (2023) 118693, http://dx.doi.org/10.1016/j.actamat.2023.118693, URL https://www.sciencedirect.com/science/article/pii/S1359645423000253.

[82] J.C. Stinville, N. Vanderesse, F. Bridier, P. Bocher, T.M. Pollock, High resolution mapping of strain localization near twin boundaries in a nickel-based superalloy, Acta Mater. (ISSN: 1359-6454) 98 (2015) 29–42, http://dx.doi.org/10.1016/j.actamat.2015.07.016, URL http://www.sciencedirect.com/science/article/pii/S1359645415004784.

[83] Wujun Yin, Fabien Briffod, Haoyu Hu, Takayuki Shiraiwa, Manabu Enoki, Three-dimensional configuration of crystal plasticity in stainless steel assessed by high resolution digital image correlation and confocal microscopy, Int. J. Plast. (ISSN: 0749-6419) 170 (2023) 103762, http://dx.doi.org/10.1016/j.ijplas.2023.103762, URL https://www.sciencedirect.com/science/article/pii/S0749641923002462.

[84] Mohammadreza Yaghoobi, Zhe Chen, Aeriel D. Murphy-Leonard, Veera Sundararaghavan, Samantha Daly, John E. Allison, Deformation twinning and detwinning in extruded Mg-4Al: In-situ experiment and crystal plasticity simulation, Int. J. Plast. (ISSN: 0749-6419) 155 (2022) 103345, http://dx.doi.org/10.1016/j.ijplas.2022.103345, URL https://www.sciencedirect.com/science/article/pii/S0749641922001267.

[85] Haoyu Hu, Fabien Briffod, Takayuki Shiraiwa, Manabu Enoki, Automated slip system identification and strain analysis framework using high-resolution digital image correlation data: Application to a bimodal Ti-6Al-4V alloy, Int. J. Plast. (ISSN: 0749-6419) 166 (2023) 103618, http://dx.doi.org/10.1016/j.ijplas.2023.103618, URL https://www.sciencedirect.com/science/article/pii/S0749641923001043.

[86] R.E. Kubilay, W.A. Curtin, Theory of twin strengthening in fcc high entropy alloys, Acta Mater. (ISSN: 1359-6454) 216 (2021) 117119, http://dx.doi.org/10.1016/j.actamat.2021.117119, URL https://www.sciencedirect.com/science/article/pii/S1359645421004997.

[87] Sun Ig Hong, C. Laird, Mechanisms of slip mode modification in F.C.C. solid solutions, Acta Metall. Mater. (ISSN: 0956-7151) 38 (8) (1990) 1581–1594, http://dx.doi.org/10.1016/0956-7151(90)90126-2, URL https://www.sciencedirect.com/science/article/pii/0956715190901262.

[88] F. Di Gioacchino, T.E.J. Edwards, G.N. Wells, W.J. Clegg, A new mechanism of strain transfer in polycrystals, Sci. Rep. (ISSN: 2045-2322) 10 (1) (2020) 10082, http://dx.doi.org/10.1038/s41598-020-66569-7.

[89] Zbigniew Stanislaw Basinski, William Hume-Rothery, The instability of plastic flow of metals at very low temperatures, Proceedings of the Royal Society of London. Series A. Mathematical and Physical Sciences 240 (1221) (1957) 229–242, http://dx.doi.org/10.1098/rspa.1957.0079, arXiv:https://royalsocietypublishing.org/doi/pdf/10.1098/rspa.1957.0079, URL https://royalsocietypublishing.org/doi/abs/10.1098/rspa.1957.0079.

[90] A. Heinz, P. Neumann, Crack initiation during high cycle fatigue of an austenitic steel, Acta Metall. Mater. (ISSN: 0956-7151) 38 (10) (1990) 1933–1940, http://dx.doi.org/10.1016/0956-7151(90)90305-Z, URL http://www.sciencedirect.com/science/article/pii/095671519090305Z.

[91] Jonathan M. Hestroffer, Marat I. Latypov, Jean-Charles Stinville, Marie-Agathe Charpagne, Valery Valle, Matthew P. Miller, Tresa M. Pollock, Irene J. Beyerlein, Development of grain-scale slip activity and lattice rotation fields in Inconel 718, Acta Mater. (ISSN: 1359-6454) 226 (2022) 117627, http://dx.doi.org/10.1016/j.actamat.2022.117627, URL https://www.sciencedirect.com/science/article/pii/S1359645422000118.